

Spin-orbital-lattice entanglement in the ideal $j = 1/2$ compound K_2IrCl_6

P. Warzanowski,¹ M. Magnaterra,¹ Ch. J. Sahle,² M. Moretti Sala,³ P. Becker,⁴ L. Bohatý,⁴ I. Císařová,⁵ G. Monaco,⁶ T. Lorenz,¹ P.H.M. van Loosdrecht,¹ J. van den Brink,^{7,8} and M. Grüninger¹

¹*Institute of Physics II, University of Cologne, 50937 Cologne, Germany*

²*ESRF, The European Synchrotron, 71 Avenue des Martyrs, CS40220, 38043 Grenoble Cedex 9, France*

³*Dipartimento di Fisica, Politecnico di Milano, I-20133 Milano, Italy*

⁴*Sect. Crystallography, Institute of Geology and Mineralogy,*

University of Cologne, 50674 Cologne, Germany

⁵*Department of Inorganic Chemistry, Charles University in Prague, 128 43 Prague 2, Czech Republic*

⁶*Dipartimento di Fisica e Astronomia "Galileo Galilei", Università di Padova, I-35121 Padova, Italy*

⁷*Institute for Theoretical Solid State Physics, IFW Dresden, 01069 Dresden, Germany*

⁸*Institute for Theoretical Physics and Würzburg-Dresden Cluster of Excellence ct.qmat,*

Technische Universität Dresden, 01069 Dresden, Germany

(Dated: July 16, 2024)

Mott insulators with spin-orbit entangled $j = 1/2$ moments host intriguing magnetic properties. The $j = 1/2$ wave function requires cubic symmetry, while a noncubic crystal field mixes $j = 1/2$ and $3/2$ character. Spectroscopic studies of $5d^5$ iridates typically claim noncubic symmetry, e.g., based on a splitting of the excited $j = 3/2$ quartet. A sizable splitting is particularly puzzling in antiferroite-type K_2IrCl_6 , a frustrated fcc quantum magnet with global cubic symmetry. It raises the fundamental question about the stability of $j = 1/2$ moments against magneto-elastic coupling. Combining resonant inelastic x-ray scattering with optical spectroscopy, we demonstrate that the multi-peak line shape in K_2IrCl_6 reflects a vibronic character of the $j = 3/2$ states rather than a noncubic crystal field. The quasimolecular crystal structure with well separated IrCl_6 octahedra explains the existence of well-defined sidebands that are usually smeared out in solids. Our results highlight the spin-orbital-lattice entangled character of cubic K_2IrCl_6 with ideal $j = 1/2$ moments.

I. INTRODUCTION

The entanglement of spin and orbital degrees of freedom via strong spin-orbit coupling leads to a multitude of novel quantum magnetic phases in $4d$ and $5d$ transition-metal compounds [1–7]. Particular interest has focused on the physics of $j = 1/2$ moments in $4d^5$ Ru^{3+} and $5d^5$ Ir^{4+} compounds. Despite strong spin-orbit coupling, these allow for isotropic Heisenberg exchange in 180° corner-sharing bonding geometry but also yield Ising exchange in 90° edge-sharing configuration [8], opening the door for the realization of Kitaev spin liquids with bond-directional exchange [9, 10] on tricoordinated lattices. Such local $j = 1/2$ moments are formed by, e.g., t_{2g}^5 Ir^{4+} ions in octahedral configuration. Resonant inelastic x-ray scattering (RIXS) at the Ir L_3 edge is a sensitive tool to test the $j = 1/2$ character, probing excitations to the $j = 3/2$ quartet, i.e., the spin-orbit exciton. A noncubic crystal-field contribution Δ_{CF} lifts the degeneracy of the quartet, see Fig. 1(c), giving rise to an admixture of $j = 3/2$ character to the $j = 1/2$ ground state wavefunction [11]. In Ir^{4+} materials, RIXS typically detects such deviations from pure $j = 1/2$ character with crystal-field splittings of roughly 0.1 eV [12–26].

Surprisingly, a sizable splitting of the $j = 3/2$ states has even been reported for compounds that are found to exhibit cubic symmetry in x-ray diffraction such as the double perovskite $\text{Ba}_2\text{CeIrO}_6$ and the antiferroite-type halides K_2IrX_6 ($X = \text{Cl}, \text{Br}$) [15, 16, 27–33]. The halides show such splitting in Ir L -edge RIXS, Raman spectroscopy, and infrared absorption [29–32]. All

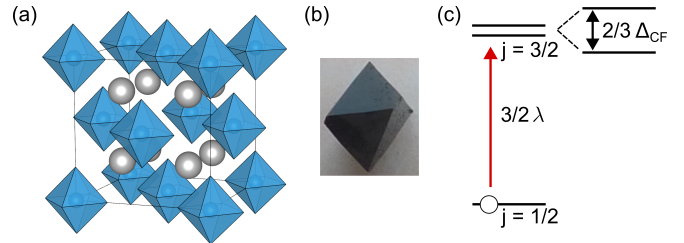


FIG. 1. (a) Sketch of the cubic crystal structure of K_2IrCl_6 with well separated IrCl_6 octahedra (blue). The K^+ ions are shown in gray. (b) Example of a grown single crystal of K_2IrCl_6 . (c) The spin-orbit exciton denotes the excitation from the local $j = 1/2$ ground state to the $j = 3/2$ excited state. In cubic symmetry, the energy equals 1.5λ . The degeneracy of the quartet is lifted in a noncubic crystal field.

three compounds host the local moments on an fcc lattice, giving rise to highly frustrated quantum magnetism where a spin-liquid phase emerges in the phase diagram based on the geometric frustration of antiferromagnetic nearest-neighbor Heisenberg exchange augmented by next-nearest-neighbor exchange [16, 34]. Remarkably, finite antiferromagnetic Kitaev exchange in this case reduces the magnetic frustration and stabilizes long-range magnetic order [16, 28, 30]. However, the pronounced frustration on the fcc lattice can be lifted via magneto-elastic coupling, where even small lattice distortions may cause strong variation of nearest-neighbor exchange couplings [16]. Such small distortions may be reconciled with an apparent global cubic structure in diffraction exper-

iments if distortions are essentially local and exhibit a very short correlation length. This raises the fundamental question on the stability of cubic $j = 1/2$ moments in frustrated quantum magnets.

Recently, Iwahara and Furukawa [35] suggested an alternative scenario for K_2IrCl_6 in which the two-peak structure of the spin-orbit exciton observed in RIXS is attributed to the interplay of spin-orbit coupling and electron-phonon coupling that gives rise to vibronic sidebands, i.e., spin-orbital-lattice entangled states with a mixed vibrational-electronic character. This scenario of a dynamic Jahn-Teller effect in the $j = 3/2$ excited state [5, 36] does not require a local breaking of cubic symmetry in the ground state and hence reconciles the spectroscopic data with the cubic symmetry reported in diffraction [27–29] and in electron spin resonance, where an isotropic g factor is found [33]. However, this explanation raises the puzzling question why distinct vibronic sidebands thus far have not been reported in the compelling series of experimental L -edge RIXS studies of other $5d^5$ Ir^{4+} oxides and halides [12–25, 37]. Based on the excellent energy resolution of optical spectroscopy, vibronic sidebands of the spin-orbit exciton have been observed in optical data of the $4d^5$ $j = 1/2$ Kitaev material $\alpha\text{-RuCl}_3$ [38, 39]. Furthermore, a dressing of the spin-orbit exciton with phonon sidebands has been claimed in oxygen K -edge RIXS on the related Kitaev material $\alpha\text{-Li}_2\text{IrO}_3$ [40]. Compared to L -edge RIXS, however, RIXS at the O K edge is much more sensitive to vibrational features due to the very different character of the intermediate state in the scattering process and the much longer core hole life time. This has recently been demonstrated for $5d^1$ $\text{Ba}_2\text{NaOsO}_6$ [41] and is further exemplified by the observation of an entire ladder of strong phononic peaks in $\alpha\text{-Li}_2\text{IrO}_3$ at the O K edge [40] and the absence of any phononic features in L -edge RIXS of the same compound [42]. Beyond iridates, the observation of vibronic sidebands of electronic excitations by means of transition-metal L -edge RIXS has been claimed in $3d^9$ $\text{Ca}_2\text{Y}_2\text{Cu}_5\text{O}_{10}$ [43], $4d^4$ K_2RuCl_6 [44, 45], and $5d^1$ A_2MgReO_6 ($A = \text{Ca}, \text{Sr}, \text{Ba}$) [46] but the observed features are broad and individual sidebands are not or hardly resolved. This is the typical situation in solids. While molecules like O_2 exhibit distinct vibronic sidebands of electronic excitations [47], in solids the existence of many different phonon modes and their dispersion smear out the sideband structure, most often turning the line shape into a broad hump even in optical data [48–51]. Remarkably, individual vibronic sidebands have been resolved in optical data of quasimolecular crystals such as K_3NiO_2 with isolated NiO_2 units [49], and the same characteristic features have been detected recently in optical data of the sister compounds K_2ReCl_6 and K_2OsCl_6 [52, 53].

Here, we join forces of RIXS and optical spectroscopy to thoroughly study the spin-orbit exciton in K_2IrCl_6 . Phenomenologically, the two-peak structure seen in RIXS can be explained by either a noncubic crystal field or a

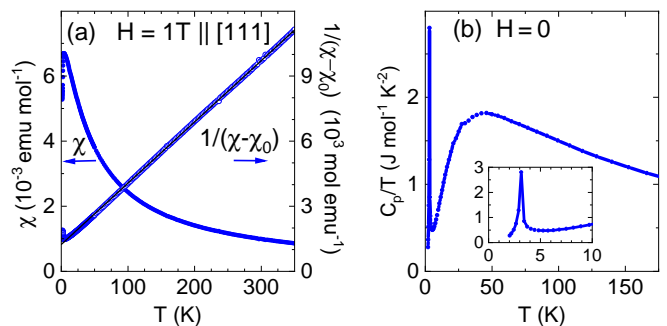


FIG. 2. (a) The magnetic susceptibility χ of K_2IrCl_6 exhibits Curie-Weiss behavior as seen by the straight line of $1/(\chi - \chi_0)$ (right axis) with $\chi_0 = -3.9 \times 10^{-5}$ emu/mol representing the sum of core diamagnetism and Van Vleck paramagnetism. The linear fit (black) above 100 K yields a Weiss temperature $\theta_W = -43.9$ K and an effective magnetic moment $\mu_{\text{eff}} = 1.69 \mu_B$. (b) The specific heat shows a pronounced peak signaling anti-ferromagnetic order at $T_N = 3.1$ K, as plotted on an enlarged scale in the inset.

vibronic picture. In contrast, the excellent energy resolution of the optical data allows us to resolve a multi-peak structure that highlights the vibronic origin, respecting cubic symmetry. These excitations are particularly well defined in K_2IrCl_6 due to its quasimolecular crystal structure with spatially isolated IrCl_6 octahedra. The competition of spin-orbit coupling and electron-phonon coupling gives rise to a dynamic Jahn-Teller effect in the $j = 3/2$ excited state, hybridizing the spin-orbit exciton with vibrational states [35]. Empirically, the overall line shape of these spin-orbital-lattice entangled excitations can be described by the Franck-Condon approximation, where the eigenstates are product states of electronic and vibrational states. However, the spin-orbital-lattice entangled nature is evident in the parameters, in particular in the peak splitting and its temperature dependence. We further demonstrate that the contribution of elementary phonon excitations in Ir L_3 -edge RIXS is negligible in K_2IrCl_6 . In contrast, the vibronic "phonon" sidebands of the spin-orbit exciton contribute in a direct RIXS process and are resonantly enhanced due to the electronic part of the wave function. Finally, we observe the double spin-orbit exciton at 1.3 eV in $\sigma_1(\omega)$ which also shows vibronic sidebands. Our results firmly establish the spin-orbital-lattice entangled nature of $j = 3/2$ excited states in cubic K_2IrCl_6 with ideal $j = 1/2$ moments.

II. EXPERIMENTAL

High-quality single crystals were grown from a solution of commercially available K_2IrCl_6 in ≈ 5.2 molar HCl by controlled evaporation of the solvent at 293 K. Within typical growth periods of two weeks, crystals of dimensions up to $1 \times 1 \times 2$ mm³ were obtained, see Fig. 1(b). In single-crystal x-ray diffraction measurements performed at ten different temperatures from 120 to 290 K, we find

the cubic space group $Fm\bar{3}m$ (Nr. 225) and lattice constants $a = 9.7458(2)$ Å (290 K) and $9.6867(3)$ Å (120 K), see Appendix A. Our x-ray diffraction results agree very well with earlier data measured at 80 and 200 K on samples of the same batch [27]. A thorough analysis of the x-ray diffraction data supports the high sample quality with no indication of a significant amount of vacancies, see also Ref. [27]. Measurements of the magnetic susceptibility χ and the specific heat C_p (see Fig. 2) yield results that agree with previous reports [28, 29, 33, 54], e.g., concerning the Néel temperature $T_N = 3.1$ K, the Weiss temperature $\theta_W = -43.9$ K, the sizable frustration parameter $f = |\theta_W|/T_N \approx 14$, and the effective magnetic moment $\mu_{\text{eff}} = 1.69 \mu_B$. The latter is in good agreement with the value $2\sqrt{j(j+1)} \mu_B \approx 1.73 \mu_B$ expected for an ideal $j = 1/2$ ground state in a cubic environment.

RIXS spectra were measured at the Ir L_3 edge at beamline ID20 of the European Synchrotron Radiation Facility. In order to resonantly enhance the spin-orbit exciton, we tuned the energy of the incident photons to 11.214 keV where an energy resolution of 25 meV was achieved [55, 56]. RIXS data were collected at 10, 100, 200, and 300 K on a (111) surface with (001) and (110) lying in the horizontal scattering plane. The incident x-ray photons were π polarized. The RIXS spectra at different temperatures have been normalized by the spectral weight of the spin-orbit exciton. The transferred momentum \mathbf{q} is given in reciprocal lattice units. Furthermore, we study the linear optical response of K_2IrCl_6 in the range from 0.1 to 6 eV, i.e., from the infrared up to the UV. Using a Woollam VASE ellipsometer from 1 to 6 eV, we address the optical response above the Mott gap at 300 K. For cubic symmetry, such ellipsometric measurements directly yield the optical conductivity $\sigma_1(\omega)$ [57]. Due to inversion symmetry on the Ir site, the spin-orbit exciton in optics corresponds to a parity-forbidden excitation. However, it acquires finite spectral weight in a phonon-assisted process. For frequencies below the Mott gap, measurements of the infrared transmittance $T(\omega)$ are ideally suited to study such weak absorption features in transparent single crystals of appropriate thickness [51], as recently demonstrated on the sister compounds K_2OsCl_6 and K_2ReCl_6 [52, 53]. For K_2IrCl_6 , we studied single-crystalline samples with a thickness $d = 380(8)$ μm , $95(3)$ μm , and $46(3)$ μm . Infrared transmittance data were measured from 0.15 to 1.85 eV with an energy resolution of 8 cm^{-1} ($\approx 1 \text{ meV}$) using a Bruker IFS 66 v/S Fourier-transform infrared spectrometer equipped with a continuous-flow ^4He cryostat.

III. SPIN-ORBIT EXCITON IN RIXS

The hallmark excitation of a local $j = 1/2$ ground state is the spin-orbit exciton, i.e., the excitation to the $j = 3/2$ quartet that is expected at 1.5λ in cubic symmetry [8, 11], where λ is the spin-orbit coupling constant, see sketch in Fig. 1(c). RIXS data of K_2IrCl_6 , measured up to 1.3 eV

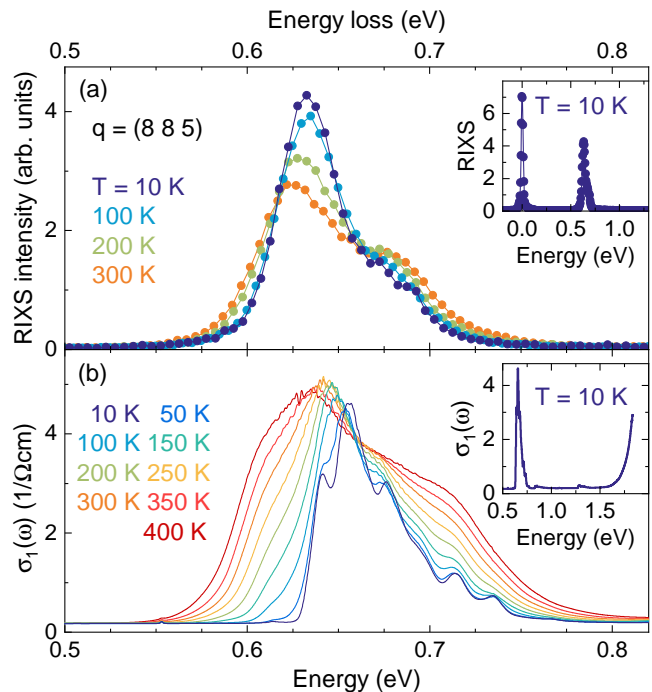


FIG. 3. Spin-orbit exciton in L_3 -edge RIXS and optics. (a) RIXS spectra at $\mathbf{q} = (8\ 8\ 5)$ show a two-peak structure around 0.63 eV. Inset: RIXS data over the entire measured range. The spin-orbit exciton is the only inelastic feature. (b) Optical conductivity $\sigma_1(\omega)$ in the same energy range as used in (a). The shift of the peak energy compared to RIXS at 10 K, the existence of several sidebands, and the increase of the spectral weight with increasing temperature highlight the phonon-assisted character. Inset: The steep onset of excitations across the Mott gap is observed at about 1.7 eV at 10 K.

with transferred momentum $\mathbf{q} = (8\ 8\ 5)$, show the spin-orbit exciton around 0.63 eV, see Fig. 3(a). The absence of further inelastic features in this energy range demonstrates the pure Ir^{4+} valence of the compound, see inset of Fig. 3(a). The narrow line width is typical for local, weakly interacting $j = 1/2$ moments [12–21], while broader, dispersive features are observed in compounds with larger exchange interactions such as Sr_2IrO_4 and $\text{Sr}_3\text{Ir}_2\text{O}_7$ [22–26]. In agreement with previous RIXS data on K_2IrCl_6 measured with 35 meV resolution [29], we observe a two-peak structure of the spin-orbit exciton. The main peak at 0.63 eV features a weak shoulder that is about 0.05 eV higher in energy, see Fig. 4. The relative intensity of this shoulder increases with increasing temperature, see Fig. 3(a), in agreement with previous results for 10 and 300 K [29]. Similar two-peak structures were reported in L -edge RIXS on the sister compounds K_2IrBr_6 and $(\text{NH}_4)_2\text{IrCl}_6$, also in their cubic phases [29, 30]. Furthermore, a splitting of the spin-orbit exciton in K_2IrCl_6 has been observed in Raman scattering [31] and in infrared absorption at room temperature [32].

In fact, such a splitting of the spin-orbit exciton is a common feature in RIXS studies on Ir^{4+} compounds, see,

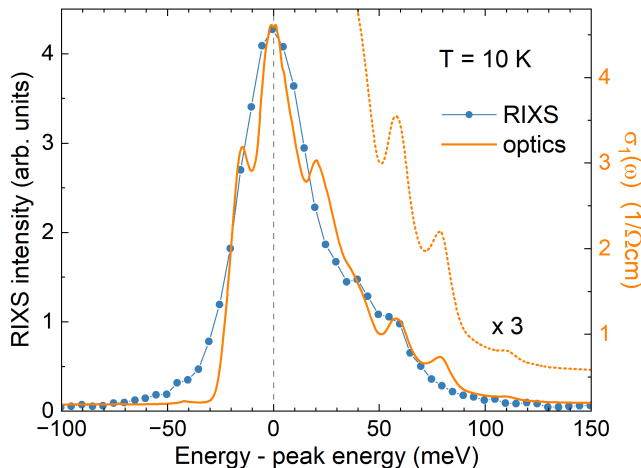


FIG. 4. Spin-orbit exciton at 10 K. The overall line shape is similar in RIXS (blue) and optics (orange, right axis). The optical conductivity shows a superposition of phonon-assisted excitations with different phonon energies, which effectively mimics the larger energy resolution of 25 meV in RIXS (see main text). For the comparison, both data sets have been shifted by the respective peak energy (633 meV for RIXS, 656 meV for $\sigma_1(\omega)$) to roughly compensate for the phonon shift. Dotted line: $\sigma_1(\omega)$ multiplied by 3 to emphasize the weak features at 0.735 and 0.766 eV, which are 0.08 and 0.11 eV above the main peak.

e.g., Refs. [12–26]. Typically, the splitting is attributed to a noncubic crystal field contribution Δ_{CF} that lifts the degeneracy of the $j=3/2$ quartet. For a single site and assuming a tetragonal distortion, the physics is described by [11]

$$\mathcal{H}_{\text{single}} = \lambda \mathbf{S} \cdot \mathbf{L} + \Delta_{\text{CF}} L_z^2 \quad (1)$$

where L_z is the component of the angular momentum \mathbf{L} along the tetragonal axis. A finite $\Delta_{\text{CF}} \ll \lambda$ lifts the degeneracy of the $j=3/2$ quartet, resulting in an experimental peak splitting $\Delta_{\text{exp}} = \frac{2}{3}\Delta_{\text{CF}}$. Following this scenario, we empirically fit the RIXS spectra with a sum of two Voigt profiles. At 10 K, the fit yields peak energies of 0.635 and 0.676 eV, see Appendix B. Solving Eq. (1), we find $\lambda = 434(1)$ meV and two possible values $\Delta_{\text{CF}} = 62$ meV and -58 meV for elongation and compression of the octahedra, respectively.

However, a finite value of the noncubic crystal field splitting $\Delta_{\text{CF}} \neq 0$ is in conflict with the globally cubic structure observed in x-ray and neutron diffraction experiments [27–29] as well as with the isotropic g factor found in an ESR study [33]. There are two scenarios to resolve this apparent discrepancy. (i) Cubic symmetry is broken locally in the initial state of the excitation process. (ii) A vibronic character of the Jahn-Teller active $j=3/2$ excited states [5, 35, 36] yields sidebands while the cubic symmetry of the ground state is preserved.

In scenario (i), local deviations from cubic symmetry may be caused by either static defects or a strong magneto-elastic coupling that triggers distortions [16].

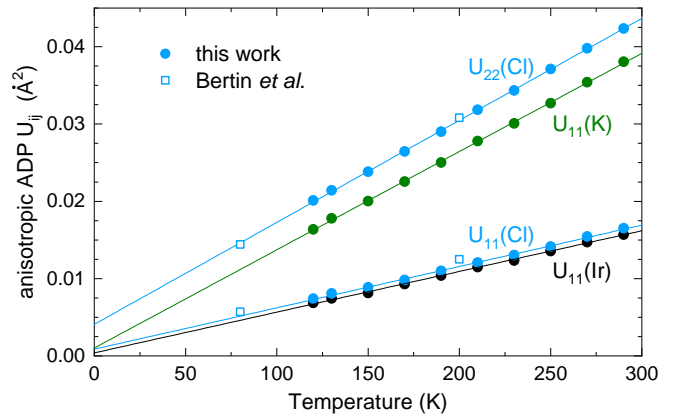


FIG. 5. Anisotropic atomic displacement parameters (ADP) U_{ij} as determined by single-crystal x-ray diffraction. Error bars are plotted but are smaller than the symbol size. Data at 80 and 200 K (open symbols) have been taken from Bertin *et al.* [27]. The lines are guides to the eye.

The latter can be reconciled with global cubic symmetry if the correlation length is small. Based on the short time scale of the RIXS process, also the thermal occupation of low-lying phonon modes effectively may break the cubic symmetry on the Ir site in the initial state [30]. In fact, x-ray studies reported comparably large atomic displacement parameters (ADPs) in the K_2PtCl_6 -type antiferrofluorite halides A_2MX_6 in general and also in K_2IrCl_6 [27, 28]. Using a cubic crystal structure in the analysis of the x-ray data, such large ADPs in general may reflect local disorder or dynamical effects such as the thermal population of low-energy phonon modes. Based on a thorough analysis of the x-ray diffraction data, Bertin *et al.* [27] conclude that there is no indication for local disorder in K_2IrCl_6 . Note that neighboring MX_6 or IrCl_6 octahedra are not connected in A_2MX_6 or K_2IrCl_6 , see Fig. 1(a), i.e., they do not share a common ligand. This causes a rotational instability and low-energy librational modes [28, 58–60]. For the halide ions, the largest ADPs indeed are found perpendicular to the Ir-Cl bonds [27, 28], as expected for a predominantly rigid rotation of the octahedra in contrast to a local, noncubic distortion away from octahedral symmetry. To scrutinize this scenario of a dynamical origin for our samples, we studied the temperature dependence of the ADPs U_{ij} of the Ir, K, and Cl ions in the range from 120 to 290 K via single-crystal x-ray diffraction measurements, see Appendix A. The results are plotted in Fig. 5 and agree very well with previous data reported for 80 and 200 K that were collected on samples from the same batch [27]. For the Cl ions, U_{11} and U_{22} refer to the displacement along and perpendicular to an Ir-Cl bond, respectively. We find $U_{22}(\text{Cl}) \gg U_{11}(\text{Cl})$, in agreement with Refs. [27, 28]. Using $\tan \varphi = \sqrt{U_{22}(\text{Cl})}/d$, we estimate the largest rotation angle $\varphi \approx 5^\circ$ at 300 K. The temperature dependence strongly supports a predominantly dynamical origin of the large U_{ij} . Above 120 K, we find a linear behavior for

all U_{ij} that extrapolates to small values at low temperature, in agreement with data reported by Khan *et al.* [28]. The data do not provide any evidence for a static contribution of local distortions or defects. A more precise quantitative determination of a possible small static contribution present already at very low temperatures requires to consider zero point fluctuations [61] and a possible temperature dependence of the phonon energies. This is beyond the scope of our study. In comparison, the cubic double perovskite $\text{Ba}_2\text{CeIrO}_6$ exhibits a much smaller temperature dependence of the ADPs, with $U_{22}(\text{O}) = 0.022 \text{ \AA}^2$ at 100 K and 0.024 \AA^2 at 300 K [16]. This suggests static disorder that may be explained by the presence of a few percent of Ce-Ir site disorder [16]. In K_2IrCl_6 , the pronounced temperature dependence of the U_{ij} is in striking contrast to the much smaller temperature dependence of the peak splitting in RIXS. We conclude that the sizable atomic displacement parameters at elevated temperature have a dynamical origin. In particular, $U_{22}(\text{Cl})$ predominantly can be attributed to rigid rotations of the octahedra.

Thermal population of low-energy rotations of the octahedra preserves cubic symmetry on average. For spectroscopy, however, it may break the cubic symmetry on the Ir site if the time scale of the electronic excitation is short enough. Nevertheless, only a small effect is expected for a rigid rotation of the octahedra. More precisely, Khan *et al.* [30] predict a dynamical rotation angle of about 5° in the cubic phase of the sister compound K_2IrBr_6 above 170 K, similar to the value that we find for K_2IrCl_6 , as discussed above. This, however, is expected to cause a noncubic crystal-field splitting of less than 10 meV at high temperature [30], which is by far not large enough to explain the splitting observed in RIXS. In particular, a thermal population of low-energy octahedral rotations cannot explain the presence of high-energy sidebands already at 10 K.

A survey of many compounds of the AMX_6 antiferroite family reveals a clear correlation between the Goldschmidt tolerance factor t and the structural transition temperature T_s from the high-temperature cubic phase to a phase with lower symmetry [27]. The Goldschmidt tolerance factor t is based on the atomic radii and usually provides a criterion for rotational phase transition in perovskites. For the antiferroite halides, Bertin *et al.* [27] find a critical value of $t \approx 1$ below which a rotational phase transition occurs, where T_s increases linearly with t decreasing below 1. For K_2IrCl_6 , the tolerance factor amounts to 1.0019 [27], in agreement with the observation of cubic symmetry down to at least 0.3 K [28, 29].

Local distortions may also result from strong magnetoelastic coupling that has been proposed based on very similar results for the double perovskite $\text{Ba}_2\text{CeIrO}_6$ [16], another compound with $j = 1/2$ moments forming an fcc lattice. Also $\text{Ba}_2\text{CeIrO}_6$ shows global cubic symmetry in x-ray diffraction measurements while RIXS reveals a splitting of the spin-orbit exciton of about 0.1 eV [15, 16], roughly a factor two larger than in K_2IrCl_6 . Exchange

couplings on the fcc lattice are highly frustrated, and this frustration may be lifted by small distortions [16]. Such distortions may escape detection in diffraction experiments if they are either very small or show a short correlation length. According to Iwahara and Furukawa [35], an interpretation of the two-peak line shape of the spin-orbit exciton of K_2IrCl_6 in terms of a static crystal-field splitting requires a displacement of the Cl ligands of $\delta r = 0.007 \text{ \AA}$. Such distortions would cause deviations from the cubic structure, but corresponding Bragg peaks have not been found [27–29]. Using a cubic structure in the analysis of diffraction data, deviations from cubic symmetry can also be detected via anomalously large atomic displacement parameters. However, effects as small as $(\delta r)^2 < 10^{-4} \text{ \AA}^2$ cannot be detected in the ADPs. Altogether, the structural data do not provide any evidence for deviations from cubic symmetry. On the contrary, a thorough analysis of the x-ray diffraction data (see also Ref. [27]) and the temperature dependence of the ADPs rather support cubic symmetry. Small distortions nevertheless cannot be excluded.

Scenario (ii) explains the two-peak structure of the RIXS spectra in terms of a vibronic character of the spin-orbit exciton, as recently proposed for K_2IrCl_6 [35]. Vibronic excitations emerge from the coupling between electronic and vibrational excitations [48–50]. An electronic excitation such as the spin-orbit exciton may change the charge-density distribution such that the lattice is not in its corresponding ground state, causing a series of phonon sidebands of a given electronic excitation. A basic example is given by the phonon satellite lines observed in photoemission on H_2 molecules [62]. Suddenly removing an electron changes the equilibrium distance and leaves the molecule in a vibrationally excited state, i.e., the molecule rings. In K_2IrCl_6 , this vibronic scenario does not break cubic symmetry in the $j = 1/2$ ground state.

With the simple two-peak structure of the RIXS data, an unambiguous distinction between the two scenarios is challenging. To resolve the origin of the splitting in K_2IrCl_6 , we study the spin-orbit exciton with optical spectroscopy, making use of the excellent energy resolution. We will show that a vibronic character is the key to understand the peculiar spectra of K_2IrCl_6 in RIXS and optics. The vibronic sidebands reflect the hybridization of spin-orbit exciton and vibrational states, i.e., spin-orbital-lattice entanglement.

IV. SPIN-ORBIT EXCITON IN OPTICAL DATA

A. Phonon-assisted character

The optical conductivity $\sigma_1(\omega)$ in the energy range of the spin-orbit exciton is plotted in Fig. 3(b). The spin-orbit exciton is an intra- t_{2g} excitation. In $\sigma_1(\omega)$, such on-site $d-d$ excitations are parity forbidden due to the presence of inversion symmetry on the Ir site. Finite spectral weight arises in a phonon-assisted process via

the simultaneous excitation of an odd-parity phonon [48–51], which explains the complex line shape. Such weakly dipole-active excitations can be studied very well in the transparency window above the phonons and below the Mott gap, as reported recently for K_2ReCl_6 and K_2OsCl_6 [52, 53] as well as for the spin-orbit exciton in $\alpha\text{-RuCl}_3$ [38]. In K_2IrCl_6 at 10 K, we observe the onset of excitations across the Mott gap around 1.7 eV, see inset of Fig. 3(b). At the peak of the spin-orbit exciton, $\sigma_1(\omega)$ reaches values of about $5 (\Omega\text{cm})^{-1}$, which is roughly two orders of magnitude smaller than for the directly dipole-allowed intersite excitations $|d_i^5 d_j^5\rangle \rightarrow |d_i^4 d_j^6\rangle$ across the Mott gap, see Appendix C.

At 10 K, the phonon-assisted character is evident from the shift of the peak energy in $\sigma_1(\omega)$ compared to RIXS and from the increase of the spectral weight with increasing temperature [52, 63]. Despite the different excitation mechanisms, the overall line shape of the spin-orbit exciton is very similar in RIXS and $\sigma_1(\omega)$ at 10 K. This is highlighted in Fig. 4, where both data sets have been shifted by the peak energy to roughly compensate for the phonon shift. The RIXS data have been measured with an energy resolution of $\delta E = 25$ meV and show a strong main peak and smaller intensity at higher energy. Qualitatively, the optical data show a very similar behavior but resolve an additional fine structure. The corresponding subbands are due to a superposition of phonon-assisted processes for different symmetry-breaking phonon modes with phonon energies in the range of roughly 10 to 40 meV, as discussed below. This superposition enhances the overall line width despite the much better energy resolution. The assignment of the subbands provides the key to understand the character of the weaker high-energy features. To this end, we need to have a close look at the peak assignment in the optical data.

B. Assignment of phonon-assisted excitations

At 10 K, the dominant phonon-assisted peaks in $\sigma_1(\omega)$ occur at $E_0 + E_{\text{odd}}$, where $E_0 = 635$ meV is the energy of the bare electronic spin-orbit exciton while E_{odd} denotes the energy of a symmetry-breaking phonon mode. The cubic crystal structure of K_2IrCl_6 hosts four odd-symmetry optical phonon modes that have been observed at 10, 18, 23, and 41 meV in infrared spectroscopy and/or inelastic neutron scattering [32, 64–66]. Given the quasi-molecular crystal structure with separate IrCl_6 octahedra, the latter three of these modes can be viewed as the three odd-symmetry normal modes of a single IrCl_6 octahedron [48] while the fourth one is a lattice phonon mode. The main peaks in $\sigma_1(\omega)$ are well described by considering $E_{\text{odd}} = 6, 18, 27,$ and 40 meV, see peaks A–D in Fig. 6(a). Taking into account that the symmetry-breaking modes do not have to be at the Γ point, the energies show good agreement with the values reported above, lending strong support to our peak assignment.

With increasing temperature, the spectral weight of

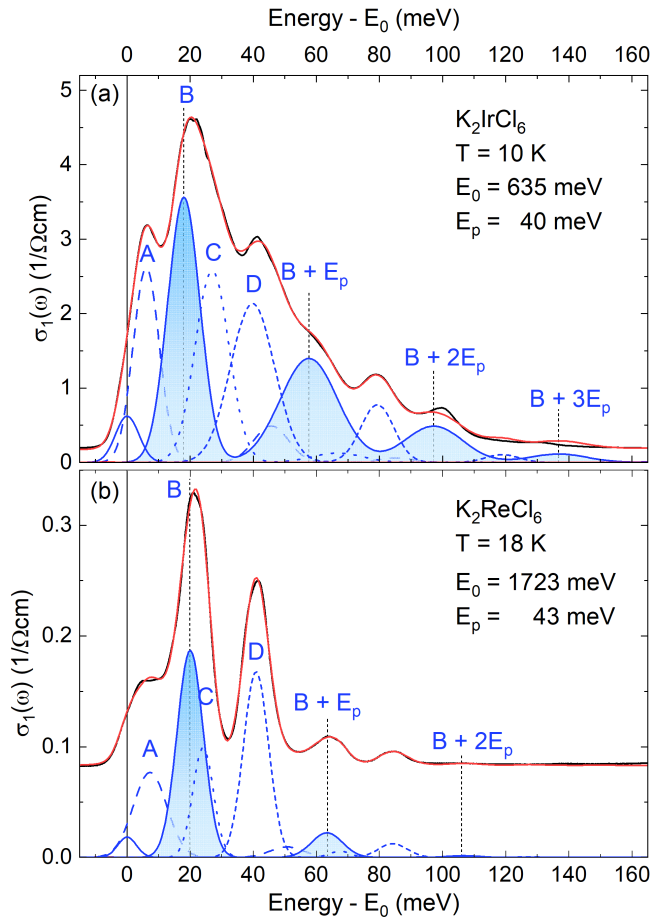


FIG. 6. Comparison of the line shape of $\sigma_1(\omega)$ for phonon-assisted intra- t_{2g} excitations in (a) K_2IrCl_6 and (b) its t_{2g}^3 sister compound K_2ReCl_6 [52]. The data (black) are shifted by the respective bare electronic energy E_0 . The similar line shape underlines the common motif of four phonon-assisted excitations A–D, each dressed by a vibronic sideband progression (see main text). For peak B, this motif is emphasized by the blue shading. Note that A–D refer to processes involving odd-symmetry phonons that yield a finite spectral weight while E_p is the energy of an even mode, see Eq. (3) and Fig. 7. The weak mode at E_0 can be attributed to a magnetic dipole transition. The red line depicts the sum of the blue curves plus a small constant offset.

a phonon-assisted process at $E_0 + E_{\text{odd}}$ increases with $1 + n(T)$, where $n(T)$ denotes the phonon occupation number of the odd-symmetry mode [48]. At finite temperatures, also phonon annihilation processes occurring at $E_0 - E_{\text{odd}}$ acquire spectral weight in $\sigma_1(\omega)$ that increases proportional to $n(T)$. The phonon-assisted character of the spin-orbit exciton in $\sigma_1(\omega)$ hence explains the different temperature dependence observed in RIXS and optics, in particular the overall increase of the spectral weight in $\sigma_1(\omega)$ with increasing temperature as well as the pronounced enhancement of absorption below E_0 .

In the chloride, the energy E_{odd} of the symmetry-breaking phonons is limited to about 40 meV. The

phonon-assisted character in $\sigma_1(\omega)$ hence explains the dominant spectral weight and the subbands in the range of roughly 0.64 to 0.68 eV. This does not yet reveal the nature of the weak features at higher energies, e.g., at 0.71, 0.74, and 0.77 eV, reaching energies as high as about $E_0 + 0.1$ eV. In general, a phonon-assisted character of the spin-orbit exciton is expected in $\sigma_1(\omega)$ as long as there is inversion symmetry on the Ir site. This phonon-assisted picture successfully has been used to describe the equivalent peaks of IrCl_6 impurities in different AMX_6 -type host compounds such as cubic Cs_2ZrCl_6 or K_2SnCl_6 [67, 68]. The data of these IrCl_6 impurities reveal the existence of vibronic sidebands. Remarkably, both the observed energies and the overall structure are very similar to our observations in single crystalline K_2IrCl_6 .

V. VIBRONIC EXCITATIONS

A. Vibronic sidebands and the Franck-Condon principle

A vibronic character emerges from the coupling of electronic excitations to vibrational degrees of freedom. An on-site intra- t_{2g} excitation may give rise to a change of the charge distribution such that the lattice is not in its ground state anymore. This yields a series of phonon sidebands of the electronic excitation [48–50] and has been claimed to describe the RIXS data of K_2IrCl_6 [35].

In fact, vibronic sidebands of on-site intra- t_{2g} excitations are a common feature in the optical conductivity of the AMX_6 family, e.g., in the sister compounds K_2ReCl_6 and K_2OsCl_6 [52, 53, 69–72]. In RIXS measurements on the Os and Re halides, however, the energy resolution was not sufficient to resolve the vibronic character [52, 53]. To put things into perspective, we consider the $5d^3$ compound K_2ReCl_6 that shows five different intra- t_{2g} excitations [52]. Optical data for one of them are depicted in Fig. 6(b). In $\sigma_1(\omega)$ of K_2ReCl_6 , the subbands are very sharp and well resolved. The stronger peaks A–D reveal the subbands of the four odd phonon modes at $E_0 + E_{\text{odd}}$, demonstrating the phonon-assisted character [52]. On top, weak vibronic sidebands are resolved at $E_0 + E_{\text{odd}} + mE_p$, where mE_p with integer m denotes the energies of a phonon progression according to the Franck-Condon principle, see Fig. 7. For the data of K_2ReCl_6 in Fig. 6(b), the electronic excited state is a Γ_7 doublet [52]. An interpretation of the high-energy sidebands in terms of crystal-field splitting is hence not applicable. These features unambiguously are of vibronic character. Remarkably, a very similar sideband structure has been observed for all five intra- t_{2g} excitations in K_2ReCl_6 [52]. This common motif also applies to the data of K_2IrCl_6 in Fig. 6(a).

The Franck-Condon principle offers a simplified, analytic, and intuitive description of the vibronic line shape. It assumes that the timescale of electronic excitations is negligible compared to phonon timescales. For an optical

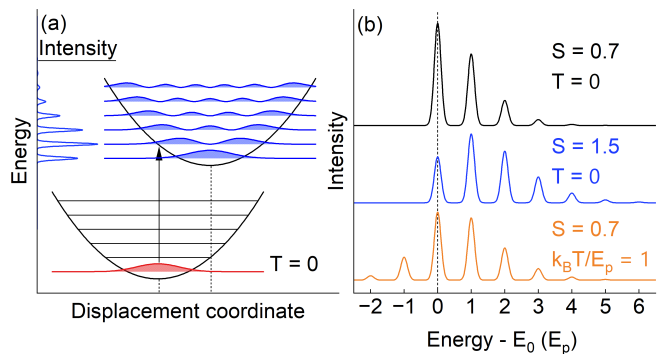


FIG. 7. Sketch of vibronic excitations in optical absorption according to the Franck-Condon principle. (a) Excitation from the ground state at $T=0$ (red) to vibronic excited states (blue). The two parabolas depict the harmonic lattice potential with phonon excitations, where the shaded area gives the squared amplitude of the wavefunction. The parabola of the electronic excited state is shifted horizontally since a change of the charge distribution affects the equilibrium positions of the ions for finite electron-phonon coupling g . The arrow corresponds to a “vertical” transition according to the Franck-Condon principle, assuming a negligible timescale for electronic excitations. On the left (blue lines), the evenly spaced comb of peaks with splitting E_p illustrates the resulting excitation spectrum. (b) Examples of the Franck-Condon line shape for different values of the Huang-Rhys factor S , see Eq. (3). The orange line corresponds to a finite temperature $T = E_p/k_B$. For clarity, the curves are offset vertically.

absorption process, this corresponds to an instantaneous, “vertical” transition from the electronic ground state to the excited state, see Fig. 7(a), where “vertical” implies no change on the horizontal axis that denotes a generalized displacement coordinate. For illustration and simplicity, we assume that there is only one odd-symmetry mode with energy E_{odd} that is relevant for the optical conductivity but not for RIXS. Furthermore, we assume that the electronic excited state is a Kramers doublet and that there is one dominant phonon mode with energy E_p that governs the progression of vibronic sidebands. Neglecting the entanglement between electronic and lattice degrees of freedom, the vibronic sidebands are shifted by mE_p in the Franck-Condon approximation, i.e., they yield an evenly spaced comb of peaks at $E_m = E_0 + E_{\text{odd}} + mE_p$ in $\sigma_1(\omega)$. At $T=0$, the line shape for optical absorption is described by [48, 73]

$$I(E) = I_0 \sum_{m=0}^{\infty} \frac{e^{-S} S^m}{m!} \delta(E_0 + E_{\text{odd}} + mE_p - E) \quad (2)$$

with $\sigma_1(E) = I(E) \cdot E$, where I_0 is proportional to the squared dipole matrix element of the (phonon-assisted) electronic transition, $e^{-S} S^m/m!$ is the Franck-Condon factor, and S is the Huang-Rhys factor, which is equivalent to the average number of phonons that are present in the excited state. It is a measure of the electron-phonon coupling constant g and governs the line shape. A large

value of S creates an envelope with a more Gaussian-like intensity distribution while a small S yields an asymmetric envelope, see Fig. 7(b). At finite temperatures, one has to consider the thermal occupation of the sideband phonon modes, $n_p = 1/[\exp(E_p/k_B T) - 1]$. The sum hence has to include negative values of m [48, 73],

$$I(E) = I_0 \sum_{m=-\infty}^{\infty} \left(\frac{n_p + 1}{n_p} \right)^{m/2} J_m \left(2S \sqrt{n_p(n_p + 1)} \right) \times e^{-S(2n_p + 1)} \delta(E_0 + E_{\text{odd}} + mE_p - E), \quad (3)$$

where J_m is the modified Bessel function of m^{th} order. For comparison with experiment, we replace the δ function in Eq. (3) with a Gaussian profile. This yields excellent agreement with $\sigma_1(\omega)$ of $5d^3$ K_2ReCl_6 , see Fig. 6(b). The experimental spectrum can be described by a superposition of such Franck-Condon progressions for all four odd-symmetry phonon modes. In K_2ReCl_6 , most of the spectral weight is in the peaks of order $m=0$ with only a small contribution of $m=1$ and basically negligible spectral weight for $m=2$. This intensity distribution corresponds to a small Huang-Rhys factor $S=0.14$. This reflects the spin-forbidden character of the excitation in K_2ReCl_6 that is observed at about $5J_H$, where J_H denotes Hund's coupling. The excitation roughly can be viewed as a flip of the spin of one electron in the t_{2g}^3 configuration, which causes only a small change of the charge distribution and corresponds to a small S . The same approach also yields an excellent description of $\sigma_1(\omega)$ of K_2IrCl_6 , see Fig. 6(a). The blue shading highlights the Franck-Condon sidebands of peak B with a larger but still small value of $S \approx 0.7$. The larger S yields detectable spectral weight of the peaks of order $m=2$ and even 3. Thereby, the vibronic model naturally explains the large number of peaks and the existence of weak features at energies as high as 0.74 and 0.77 eV, more than 0.1 eV above the bare electronic excitation energy $E_0 = 635$ meV.

Thus far we discussed the Franck-Condon approximation for an optical excitation. We claim that Eq. (3) can also be applied to vibronic sidebands of an electronic excitation studied in direct RIXS, which is supported by the overall agreement of the line shapes shown in Fig. 4. Note that the case is different for elementary phonons and multi-phonons. These are excited in an *indirect* RIXS process that can be approximated by using two Franck-Condon factors [74–77], see Sec. VD. For K_2IrCl_6 , Eq. (3) provides an excellent empirical description of our RIXS spectra, see Fig. 8. At 10 K, the fit yields $S = 0.30$, $E_p = 44$ meV, and the bare electronic energy $E_0 = 633$ meV. With an energy resolution of 25 meV, the latter agrees very well with $E_0 = 635$ meV found in $\sigma_1(\omega)$. In the next paragraph, we discuss E_p to collect evidence for the spin-orbital-lattice entangled character.

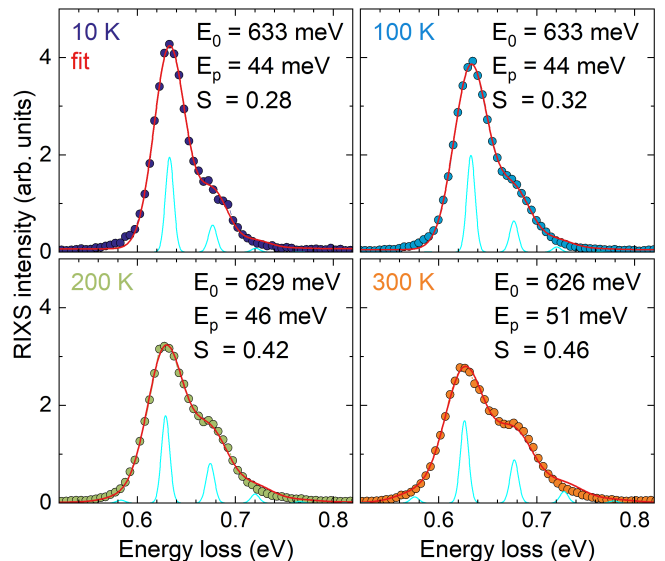


FIG. 8. Vibronic fits of the RIXS data at different temperatures using the Franck-Condon picture from Eq. (3). In each panel, we state the energy E_0 of the bare electronic excitation, the energy E_p of the phonon progression mode, and the Huang-Rhys factor S . The red lines depict the full fit. Cyan curves illustrate the phonon progression of sidebands for the same parameters with 10 meV width of the Gaussian profile and reduced total intensity.

B. Beyond the Franck-Condon approximation

The Franck-Condon principle is valuable for an intuitive explanation of the overall line shape. For a microscopic description of K_2IrCl_6 , Iwahara and Furukawa [35] treated electron-phonon coupling g and spin-orbit coupling λ on the same footing. They find that the spin-orbit exciton with its vibronic sidebands is of spin-orbital-lattice entangled character. Strictly speaking, the simple picture of the simultaneous excitation of a spin-orbit exciton and one or several phonons, causing a comb of equidistant peaks, is only applicable for $g \rightarrow 0$, in which case the intensity of the sidebands vanishes. For finite g , the excitation spectrum is more complex. Iwahara and Furukawa [35] predict a larger number of peaks but many of them are small and hard to resolve experimentally. Furthermore, hybridization shifts the energies such that the sidebands are not equidistant anymore. In K_2IrCl_6 , however, we can only determine two peak energies in RIXS, and the complex line shape of the phonon-assisted excitations in $\sigma_1(\omega)$ does not allow us to clearly identify deviations from a comb-like behavior. The hybridized character may also give rise to differences in line shape between RIXS and $\sigma_1(\omega)$, e.g., due to the presence of the symmetry-breaking phonon mode in the case of the optical data. However, we are lacking a theoretical prediction for such differences. From an experimental point of view, the hybridized character at this stage can be detected in the value of the peak splitting, which is

captured by E_p in Eq. (3).

At 10 K, the fits yield $E_p = 40$ meV in $\sigma_1(\omega)$ and 44 meV in RIXS, see Figs. 6(a) and 8. In general, the even electronic excitations may couple to phonons of a_{1g} , e_g , and t_{2g} symmetry [78], where the latter usually is neglected. The elementary phonon modes of a_{1g} and e_g symmetry have been observed in Raman scattering at 44 meV and 37 meV, respectively [31]. In the Franck-Condon approximation, the experimental splitting thus appears to suggest a predominant coupling to the a_{1g} mode, the breathing mode of the IrCl_6 octahedron. This applies if, e.g., both the electronic ground state and the excited state show cubic symmetry, which is the case for ideal $j = 1/2$ and $3/2$ states. For the doublet excited state of K_2ReCl_6 addressed in Fig. 6(b), the phonon sidebands with $E_p = 43$ meV have been attributed to the a_{1g} mode [52, 70]. However, the situation is different in K_2IrCl_6 due to the degeneracy of the excited $j = 3/2$ quartet that is lifted by coupling to the Jahn-Teller active e_g phonon mode [35]. In this case, the energy splitting between the lowest two strong RIXS peaks roughly is given by $E_p \cdot (1 + g^2/8)$. Note that g is dimensionless in the definition of Ref. [35]. With $E_p = 37$ meV for the e_g mode and $g = 1.2$, Iwahara and Furukawa find a splitting of 45 meV between the two strongest peaks in the calculated RIXS response, in excellent agreement with the experimental data at 10 K. The fact that the splitting depends on g reflects the dynamic Jahn-Teller effect, lifting the degeneracy of the $j = 3/2$ quartet. This is in particular relevant for the temperature dependence of the splitting, as discussed in the next paragraph. Strictly speaking, the splitting also depends on λ due to a finite admixture of $j = 1/2$ character via the pseudo-Jahn-Teller effect [35, 79]. This, however, is small and can be neglected.

C. Temperature dependence

The convincing description of the temperature dependence of the RIXS data is a particular asset of the vibronic scenario. Using $g = 1.2$, Iwahara and Furukawa [35] showed that a vibronic model with spin-orbital-lattice entangled states describes the temperature dependence observed in RIXS. First, we address the qualitative behavior of the experimental data, see Figs. 3(a) and 8. This can be understood within the Franck-Condon picture, see Eq. (3) and the black and orange lines in Fig. 7(b). The thermal occupation of phonon modes gives rise to a redistribution of the intensity to high energies as well as to the range below the main peak, where the latter can be attributed to the emergence of a subband at $E_0 - E_p$.

As at 10 K, a quantitative analysis reveals fingerprints of the entangled character. With increasing temperature, the fit yields an increase of the peak splitting E_p and of S and a modest red shift of E_0 , see Fig. 8. Remarkably, the behavior of all three observations is in line with an increase of the electron-phonon coupling constant g . An

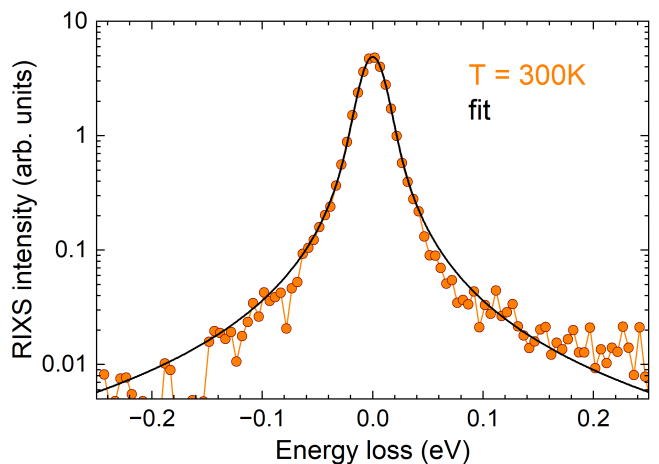


FIG. 9. RIXS data of K_2IrCl_6 around zero energy loss at 300 K. The data are plotted on a logarithmic scale to emphasize the tails of the elastic line that is fitted using a Voigt line shape with the instrumental resolution $\delta E = 25$ meV. The symmetric behavior around zero loss down to the noise level of about 0.01 provides no indication of low-energy excitations. In particular, the intensity of phonons is negligible in RIXS at the Ir L_3 edge.

increase of g enhances S and, in a spin-orbital-lattice entangled scenario [35], reduces the energy E_0 of the main peak via the dynamic Jahn-Teller effect while increasing the splitting $E_p \cdot (1 + g^2/8)$ of the dominant RIXS peaks, as discussed above. In fact, the fit yields a splitting as large as 51 meV at 300 K. This is hard to reconcile with the phonon energies of the chloride in a Franck-Condon scenario but can be attributed to the g dependence of the splitting in a spin-orbital-lattice entangled picture.

A further contribution to the 1% reduction of E_0 may originate from thermal expansion of the lattice and a corresponding increase of the Ir-Cl distance. This modifies the cubic crystal field $10Dq$ and thereby the effective value of λ . For the cubic phase of K_2IrBr_6 , the peak splitting has been reported by Khan *et al.* [30] to increase from about 50 meV at 170 K to 70 meV at 300 K, while Reig-i-Plessis *et al.* find a smaller value of 47 meV at 300 K [29]. This discrepancy may originate from the line shape of the spin-orbit exciton in K_2IrBr_6 which rather shows a subtle shoulder instead of a clear splitting.

The temperature dependence of $\sigma_1(\omega)$ predominantly reflects the phonon-assisted character, which causes a pronounced increase of the spectral weight. The many subbands visible at 10 K are smeared out at elevated temperatures, see Fig. 3(b). Therefore we refrain from fitting $\sigma_1(\omega)$ at high temperature.

D. Phonons and phonon sidebands

The observation of vibronic "phonon" sidebands is particularly interesting given the fact that the intensity of el-

elementary phonon excitations is negligible in L -edge RIXS on $5d^5$ Ir^{4+} $j=1/2$ Mott insulators [42]. For K_2IrCl_6 , this is highlighted in Fig. 9, which focuses on the RIXS response around zero loss. The data have been measured with a scattering angle 2θ close to 90° , which yields an elastic line of moderate strength. The symmetric behavior around zero loss is emphasized by a fit with a Voigt profile. The data are very well described by considering only the elastic line and do not provide any evidence for a sizable inelastic contribution below 0.1 eV. Even at 300 K, where the intensity of low-energy modes is enhanced by the Bose factor, the contribution of phonons is negligible.

In L -edge RIXS on Mott-insulating $5d^5$ iridates, spin and orbital excitations are boosted in a direct RIXS process [80]. The x-ray absorption step from the ground state to the intermediate state is followed by the x-ray emission step from the intermediate state to the final state. In general, phonons are excited with a much smaller cross section in *indirect* RIXS, i.e., via the dynamics in the *intermediate* state. In RIXS a phonon is created if the lattice distorts in the intermediate state to screen the core hole [74–77, 81]. A simplified description of phonon excitations can again be achieved in a Franck-Condon picture. However, with the coupling taking place in the intermediate state, one has to use *two* Franck-Condon factors, one for the absorption step, and the second one for x-ray emission [74–77]. For L -edge RIXS with an incident energy as large as 11.214 keV, the absence of any phonon signatures can be rationalized via the Ir $2p^5 t_{2g}^6$ intermediate state, which is well screened and shows a short life time of only a few femtoseconds. In contrast, phonon contributions can be observed in RIXS on Ir oxides at the O K edge due to the very different intermediate state [40, 74–76].

Previously, this phonon approach with two Franck-Condon factors has also been applied to vibronic sidebands of on-site d - d excitations studied in RIXS at the O K edge, e.g., in Li_2CuO_2 and $\alpha\text{-Li}_2\text{IrO}_3$ [40, 82], as well as at the Cu L edge in $\text{Ca}_2\text{Y}_2\text{Cu}_5\text{O}_{10}$ [43]. In our data of K_2IrCl_6 , measured at the Ir L_3 edge, indirect RIXS processes are negligible. The spin-orbit exciton and its vibronic sidebands are resonantly enhanced in a direct RIXS process due to the electronic contribution to the wave function. Empirically, the data are described by Eq. (3), where the squared matrix element of the electronic transition in direct RIXS yields I_0 . As in optical absorption, the electronic excitation leaves the system in a vibrationally excited state, see Fig. 7. In this sense, the coupling to the lattice occurs in the final state, in contrast to the case of elementary phonons discussed above.

VI. DOUBLE SPIN-ORBIT EXCITON

The excitation of double spin-orbit excitons in the optical conductivity around 1.3 eV provides a further example for a vibronic excitation in K_2IrCl_6 , see Fig. 10. The feature is very weak, the spectral weight being roughly

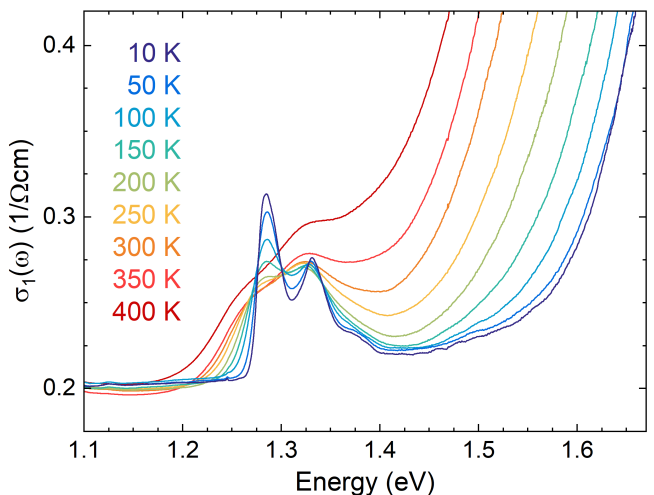


FIG. 10. Double spin-orbit exciton around 1.3 eV with vibronic sidebands. Up to about 200 K, the three-peak structure of this very weak absorption band is located right below the onset of excitations across the Mott gap.

a factor 50 smaller than for the single spin-orbit exciton, see inset of Fig. 3(b). At 10 K, the energy of the first peak $E_{2\text{SO}} = 1286 \text{ meV} = 2 \cdot 643 \text{ meV}$ is very close to twice the energy $E_0 = 635 \text{ meV}$ for the single spin-orbit exciton. This peak at 1.3 eV can hence be assigned to the simultaneous excitation of two spin-orbit excitons on neighboring sites. Double and even triple spin-orbit excitons previously have been observed in $\sigma_1(\omega)$ of the $4d^5$ $j=1/2$ compound $\alpha\text{-RuCl}_3$ [38, 39]. Similar overtones or double intra- t_{2g} excitations have also been reported in orbitally ordered YVO_3 as well as in K_2ReCl_6 and K_2OsCl_6 [52, 53, 71, 83].

The spectral weight of this feature is insensitive to temperature at least up to 200 K. At still higher temperature, it drowns in the onset of excitations across the Mott gap which shifts to lower energies with increasing temperature. The temperature-independent spectral weight suggests that this feature is *not* phonon-assisted but rather directly infrared allowed, even though with a very small spectral weight. This agrees with results on K_2ReCl_6 and K_2OsCl_6 [52, 53]. A finite dipole moment may arise if the total excited state breaks inversion symmetry on the bond. This is, e.g., the case for a spin-orbit exciton with $j_z = 3/2$ on one site but $j_z = 1/2$ on the neighboring site. At 10 K, the splitting between the main peak at $E_{2\text{SO}} = 1286 \text{ meV}$ and the first sideband amounts to 46 meV. The splitting between the second peak and the weak third peak is comparable but the large width prevents a more precise determination. The value of 46 meV is very similar to the vibronic splitting of the spin-orbit exciton, see Fig. 8, as well as to the vibronic splitting observed for the overtones in K_2ReCl_6 [52]. The line shape, the experimental peak splitting, and the analogy with the sister compound K_2ReCl_6 provide strong evidence for a vibronic character of the double spin-orbit exciton.

VII. DISCUSSION AND CONCLUSION

Spin-orbit entangled $j=1/2$ moments are Kramers doublets and as such not Jahn-Teller active. In frustrated quantum magnets, magneto-elastic coupling nevertheless may give rise to distortions that break cubic symmetry and lift magnetic frustration in $j=1/2$ compounds [16]. A possibly pronounced magneto-elastic coupling would play an essential role for the low-energy physics of $j=1/2$ quantum magnets. We combined RIXS, optical spectroscopy, and single-crystal x-ray diffraction to study the possible role of magneto-elastic coupling in antiferroite-type K_2IrCl_6 with $j=1/2$ moments on an fcc lattice with highly frustrated exchange couplings. The global cubic structure of K_2IrCl_6 is well established [27–29]. The sizable atomic displacement parameters reported for K_2IrCl_6 at elevated temperatures [27, 28] exhibit a linear temperature dependence, underlining their dynamical origin based on rigid, low-energy rotations of the IrCl_6 octahedra. Even though the diffraction data do not provide any indication for deviations from cubic symmetry, the presence of local distortions cannot fully be excluded. Small distortions are a challenge for diffraction experiments and often are detected more easily in spectroscopy based on, e.g., a change of selection rules. The two-peak structure of the spin-orbit exciton observed in L -edge RIXS around 0.63 eV can be attributed to either a noncubic crystal-field splitting or to a vibronic character with phonon sidebands. Optical spectroscopy provides complementary information based on the excellent energy resolution and the different excitation process with different selection rules. We observe a multitude of phonon-assisted peaks in $\sigma_1(\omega)$ that reach as high as 0.74 and 0.77 eV. These features require an explanation in terms of vibronic sidebands, in agreement with previous results on IrCl_6 impurities in host crystals [67, 68], with the vibronic character of the double spin-orbit exciton that we find around 1.3 eV, and with optical results on related intra- t_{2g} excitations in the sister compounds K_2ReCl_6 and K_2OsCl_6 [52, 53]. Furthermore, the vibronic picture is able to describe the temperature dependence observed in RIXS [35]. The success of the vibronic scenario suggests that magneto-elastic coupling is not decisive for the stability of the $j=1/2$ moments in K_2IrCl_6 . Altogether, we conclude that K_2IrCl_6 hosts cubic $j=1/2$ moments and spin-orbital-lattice entangled $j=3/2$ excited states.

This spin-orbital-lattice entangled nature of the spin-orbit exciton is caused by electron-phonon coupling that yields a hybridization of the Jahn-Teller active $j=3/2$ quartet with vibrational states [35]. The Franck-Condon approximation offers an analytic description of the vibronic line shape. It assumes a negligible timescale for electronic excitations, approximating the eigenstates as product states of electronic and vibrational states. Empirically, the Franck-Condon approach describes the data of RIXS and optics well and in an intuitive way. Equivalent to the analysis of optical data, a single Franck-

Condon factor is appropriate to describe vibronic excitations studied in *direct* RIXS. This differs from the case of elementary phonons that contribute in an indirect RIXS process, and we have shown that this contribution is negligible in our L -edge RIXS data of K_2IrCl_6 . This intuitively highlights the particular character of the vibronic "phonon" sidebands of the spin-orbit exciton, for which resonance enhancement in direct RIXS applies to the electronic part of the wave function.

A more detailed quantitative description of the experimental data reveals the limitations of the Franck-Condon scenario, in which the splitting is equal to the phonon energy. In particular, the large splitting of 44 meV observed at 10 K and even 51 meV at 300 K is hard to reconcile with an elementary phonon energy in K_2IrCl_6 . In contrast, a theory describing the microscopic coupling of the spin-orbit entangled states to the e_g phonon mode with energy E_p yields $E_p \cdot (1+g^2/8)$ for the splitting of the first two strong RIXS peaks [35]. We thus conclude that the large splitting and its temperature dependence are fingerprints of the spin-orbital-lattice entangled character beyond the Franck-Condon approximation.

Concerning L -edge RIXS, the well resolved vibronic sideband in K_2IrCl_6 stands out in transition-metal compounds in general as well as compared to other $5d^5$ iridates. The splittings larger than 0.1 eV observed in Ir^{4+} oxides [12, 13, 15–26] are caused by a noncubic crystal field. Vibronic sidebands of electronic excitations have been claimed in $\text{Ca}_2\text{Y}_2\text{Cu}_5\text{O}_{10}$ [43], K_2RuCl_6 [44], as well as in $5d^1$ compounds based on the asymmetric line shape of the excitation from $j=3/2$ to $1/2$ [41, 46], but individual peaks have not been resolved. Typically, the subbands of vibronic excitations are not resolved in solids, even in optical data. However, the vibronic features are particularly sharp in $\sigma_1(\omega)$ of K_2ReCl_6 [52] and still very well resolved in K_2IrCl_6 , even in RIXS. This can be attributed to the quasimolecular crystal structure with well separated $M\text{Cl}_6$ octahedra. The antiferroite-type A_2MX_6 compounds thus offer an ideal platform to further investigate the role of vibronic effects in RIXS.

APPENDIX

A. Crystal structure determination

The x-ray diffraction experiments for a crystal of K_2IrCl_6 with dimensions of $0.072 \times 0.059 \times 0.049 \text{ mm}^3$ were performed on a Bruker D8 VENTURE Kappa Duo PHOTONIII diffractometer with a $I\mu\text{S}$ micro-focus sealed tube (Mo $\text{K}\alpha$ radiation, 0.71073 Å). Using an Oxford Cryostream Cooler800, we collected data between 290 and 120 K. The crystal structure was solved by direct methods (SHELXT) [84] and refined by full matrix least squares based on F^2 (SHELXL2019) [85]. Multi-scan absorption correction was applied. The anisotropic atomic displacement parameters U_{ij} are given in Table I. The data were obtained by first cooling down in steps

T/K		$U_{11}(\text{Ir})$	$U_{11}(\text{Cl})$	$U_{22}(\text{Cl})$	$U_{11}(\text{K})$
290	I	0.01584(8)	0.0166(3)	0.0425(3)	0.0382(3)
	II	0.01557(7)	0.0164(2)	0.0422(2)	0.0379(2)
270	I	0.01466(7)	0.0153(2)	0.0397(2)	0.0353(2)
	II	0.01475(7)	0.0156(2)	0.0399(2)	0.0355(2)
250	I	0.01360(8)	0.0138(3)	0.0373(3)	0.0327(3)
	II	0.01354(7)	0.0145(2)	0.0369(2)	0.0327(2)
230	I	0.01219(6)	0.01285(18)	0.03407(17)	0.02996(17)
	II	0.01250(7)	0.0132(2)	0.0346(2)	0.0302(2)
210	I	0.01140(7)	0.0120(2)	0.0317(2)	0.0277(2)
	II	0.01157(7)	0.0121(2)	0.0320(2)	0.0279(2)
190	I	0.01035(6)	0.0110(2)	0.02898(19)	0.02500(19)
	II	0.01045(7)	0.0110(2)	0.0290(2)	0.0250(2)
170	I	0.00930(6)	0.00981(19)	0.02660(18)	0.02249(17)
	II	0.00931(7)	0.0098(2)	0.0263(2)	0.0226(2)
150	I	0.00836(6)	0.0090(2)	0.02420(18)	0.02019(18)
	II	0.00793(5)	0.00871(16)	0.02343(14)	0.01984(14)
130	I	0.00759(12)	0.0082(3)	0.0216(3)	0.0180(3)
	II	0.00729(6)	0.00797(19)	0.02123(17)	0.01761(16)
120	I	0.00686(6)	0.00739(19)	0.02010(17)	0.01635(16)

TABLE I. Anisotropic atomic displacement parameters U_{ij} , derived from crystal structure determination by single crystal x-ray diffraction. The data were measured in the sequence from 290 to 120 K (I) and back to 290 K (II). Figure 5 shows the average of I and II. All U_{ij} are given in units of \AA^2 .

from 290 to 120 K, while a second set of data points was measured upon heating back to 290 K.

The x-ray crystallographic data have been deposited at the Inorganic Crystal Structure Database via the joint CCDC/FIZ Karlsruhe deposition service [86] with the deposition numbers CCDC/CSD 2367387 to 2367405 and can be obtained free of charge from <https://www.ccdc.cam.ac.uk/structures>.

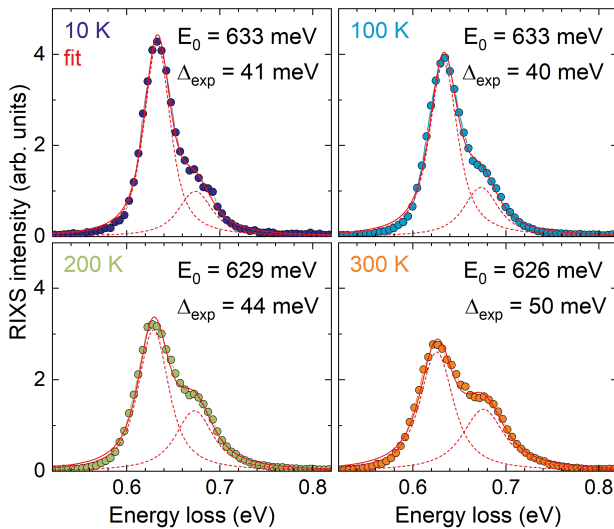


FIG. 11. Fits of the RIXS data using two Voigt profiles. The two features (dashed) are peaking at E_0 and $E_0 + \Delta_{\text{exp}}$. The solid red line depicts the sum.

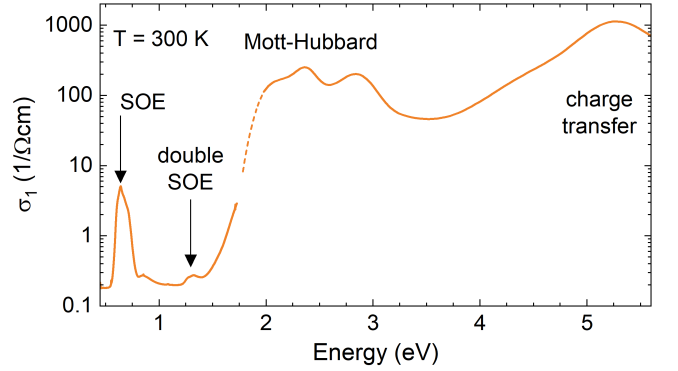


FIG. 12. Optical conductivity up to 5.6 eV at room temperature. Data above the Mott gap have been determined by ellipsometry measurements. Note the logarithmic scale. Above the Mott gap, $\sigma_1(\omega)$ is roughly two orders of magnitude larger than for the spin-orbit exciton. The dashed line depicts a fit that assumes a Tauc-Lorentz shape of the Mott gap.

B. Two-peak fit of RIXS

Phenomenologically, the apparent two-peak structure of the RIXS data can also be described by employing two oscillators with a Voigt line shape, see Fig. 11. The Voigt profile corresponds to a convolution of Gaussian and Lorentzian peaks. For the Gaussian part we use the instrumental width determined from the elastic line. These fits yield the energy E_0 of the dominant peak and the peak splitting Δ_{exp} of 40 to 50 meV. Compared to the vibronic fit shown in Fig. 8, we find the same result for E_0 while the peak splitting Δ_{exp} is slightly smaller than the phonon progression energy E_p . The agreement between the two-peak Voigt fits and the experimental data does not achieve the same quality as for the vibronic fits shown in Fig. 8. This applies in particular to the low-frequency side below 0.6 eV and reflects the extended tails of the Lorentzian contribution.

C. Optical conductivity above the Mott gap

We address the optical conductivity at higher energies to put the phonon-assisted features into context. Figure 12 shows $\sigma_1(\omega)$ above the Mott gap as determined by ellipsometry. Above about 4 eV, we observe charge-transfer excitations between Ir and Cl sites. In the energy range from 2 to 3.5 eV we find Mott-Hubbard excitations across the Mott gap, i.e., *intersite* excitations $|d_i^5 d_j^5\rangle \rightarrow |d_i^4 d_j^6\rangle$ between the Ir sites i and j . Compared to *on-site* d - d excitations such as the spin-orbit exciton, the value of $\sigma_1(\omega)$ for these directly dipole-allowed excitations is about two orders of magnitude larger. Accordingly, the strong intersite excitations cover the on-site crystal-field excitations from t_{2g} to e_g states. These are peaking in the energy range from 2.5 to 3.5 eV in RIXS on K_2IrCl_6 [29] but are not visible in the optical data. Con-

sidering the additional energy cost of the on-site Coulomb repulsion U for intersite excitations across the Mott gap, the two lowest peaks at about 2.4 and 2.9 eV have to be attributed to t_{2g} states. Their energies can be rationalized in terms of local multiplets. This approach is corroborated by the observation that the spectral weight of such intersite excitations in many transition-metal compounds reflects spin and orbital correlations between nearest neighbors [87–94]. In this picture, the lowest $|d_i^4 d_j^6\rangle$ excited states exhibit a $t_{2g}^6 {}^1A_1$ multiplet on site j while site i hosts a t_{2g}^4 multiplet with either 3T_1 or ${}^1T_2/{}^1E$ symmetry. In a t_{2g} -only picture, the corresponding excitation energies $E(t_{2g}^4) + E(t_{2g}^6) - 2E(t_{2g}^5)$ amount to $U - 3J_H$ and $U - J_H$ [95]. The energy difference of $2J_H$ is reduced to about $1.5J_H$ upon taking into account the interaction with e_g orbitals [53]. The observed energy difference of 0.5 eV thus agrees with the expectation $J_H \approx 0.3\text{--}0.4$ eV [53, 96, 97].

Finally, we want to point out the close relation to intersite excitations in d^1 compounds such as Mott insulating YTiO₃ [92]. There, the energy of the $|d_i^0 d_j^2\rangle$ excited states is governed by two-electron t_{2g}^2 multiplets that show the same symmetry as the two-hole t_{2g}^4 states discussed above for K₂IrCl₆. Remarkably, the lowest intersite excitation in YTiO₃, involving the 3T_1 multiplet, exhibits a two-peak structure that has been explained in terms of a Mott-Hubbard exciton [92] for which the energy is re-

duced by the Coulomb interaction of an electron-hole pair on nearest-neighbor sites as well as by magnetic and orbital correlations. The term Mott-Hubbard exciton is employed not only for truly bound excitons below the Mott gap but also for a nearly-bound resonance within the continuum, as observed in YTiO₃. Mott-Hubbard excitons have been discussed also for the $5d^5$ iridates Na₂IrO₃ and Sr₂IrO₄ [98, 99]. In this light, one may speculate that the pronounced shoulder at 2 eV of the peak at 2.5 eV in $\sigma_1(\omega)$ of K₂IrCl₆ also reflects nearest-neighbor Coulomb interactions.

ACKNOWLEDGMENTS

We thank K. Hopfer and H. Schwab for experimental support and the European Synchrotron Radiation Facility for providing beam time at ID20 and technical support. Furthermore, we acknowledge funding from the Deutsche Forschungsgemeinschaft (DFG, German Research Foundation) through Project No. 277146847 – CRC 1238 (projects A02, B02, B03) as well as from the European Union – Next Generation EU – “PNRR – M4C2, investimento 1.1 – Fondo PRIN 2022” – “Superlattices of relativistic oxides” (ID 2022L28H97, CUP D53D23002260006).

-
- [1] W. Witczak-Krempa, G. Chen, Y. B. Kim, and L. Balents, *Correlated Quantum Phenomena in the Strong Spin-Orbit Regime*, Annu. Rev. Condens. Matter Phys. **5**, 57 (2014).
- [2] J. G. Rau, E. Kin-Ho Lee, and H.-Y. Kee, *Spin-Orbit Physics Giving Rise to Novel Phases in Correlated Systems: Iridates and Related Materials*, Annu. Rev. Condens. Matter Phys. **7**, 195 (2016).
- [3] R. Schaffer, E. Kin-Ho Lee, B.-J. Yang, and Y. B. Kim, *Recent progress on correlated electron systems with strong spin-orbit coupling*, Rep. Prog. Phys. **79**, 094504 (2016).
- [4] H. Takagi, T. Takayama, G. Jackeli, G. Khaliullin, and S. E. Nagler, *Concept and realization of Kitaev quantum spin liquids*, Nat. Rev. Phys. **1**, 264 (2019).
- [5] S. V. Streltsov and D. I. Khomskii, *Jahn-Teller Effect and Spin-Orbit Coupling: Friends or Foes?*, Phys. Rev. X **10**, 031043 (2020).
- [6] T. Takayama, J. Chaloupka, A. Smerald, G. Khaliullin, and H. Takagi, *Spin-Orbit-Entangled Electronic Phases in 4d and 5d Transition-Metal Compounds*, J. Phys. Soc. Jpn. **90**, 062001 (2021).
- [7] D. I. Khomskii and S. V. Streltsov, *Orbital Effects in Solids: Basics, Recent Progress, and Opportunities*, Chem. Rev. **121**, 2992 (2021).
- [8] G. Jackeli and G. Khaliullin, *Mott Insulators in the Strong Spin-Orbit Coupling Limit: From Heisenberg to a Quantum Compass and Kitaev Models*, Phys. Rev. Lett. **102**, 017205 (2009).
- [9] S.H. Chun, J.-W. Kim, J. Kim, H. Zheng, C.C. Stoumpos, C.D. Malliakas, J.F. Mitchell, K. Mehlawat, Y. Singh, Y. Choi, T. Gog, A. Al-Zein, M. Moretti Sala, M. Krisch, J. Chaloupka, G. Jackeli, G. Khaliullin, and B.J. Kim, *Direct evidence for dominant bond-directional interactions in a honeycomb lattice iridate Na₂IrO₃*, Nat. Phys. **11**, 462 (2015).
- [10] M. Magnaterra, K. Hopfer, Ch. J. Sahle, M. Moretti Sala, G. Monaco, J. Attig, C. Hickey, I.-M. Pietsch, F. Breitenner, P. Gegenwart, M. H. Upton, Jungho Kim, S. Trebst, P. H. M. van Loosdrecht, J. van den Brink, and M. Grüninger, *RIXS observation of bond-directional nearest-neighbor excitations in the Kitaev material Na₂IrO₃*, arXiv:2301.08340
- [11] M. Moretti Sala, S. Boseggia, D. F. McMorrow, and G. Monaco, *Resonant X-Ray Scattering and the $j_{\text{eff}} = 1/2$ Electronic Ground State in Iridate Perovskites*, Phys. Rev. Lett. **112**, 026403 (2014).
- [12] X. Liu, V. M. Katukuri, L. Hozoi, W.-G. Yin, M. P. M. Dean, M. H. Upton, J. Kim, D. Casa, A. Said, T. Gog, T. F. Qi, G. Cao, A. M. Tsvelik, J. van den Brink, and J. P. Hill, *Testing the Validity of the Strong Spin-Orbit-Coupling Limit for Octahedrally Coordinated Iridate Compounds in a Model System Sr₃CuIrO₆*, Phys. Rev. Lett. **109**, 157401 (2012).
- [13] H. Gretarsson J. P. Clancy, X. Liu, J. P. Hill, E. Bozin, Y. Singh, S. Manni, P. Gegenwart, J. Kim, A. H. Said, D. Casa, T. Gog, M. H. Upton, H.-S. Kim, J. Yu, V. M. Katukuri, L. Hozoi, J. van den Brink, and Y.-J. Kim, *Crystal-Field Splitting and Correlation Effect on*

- the Electronic Structure of A_2IrO_3* , Phys. Rev. Lett. **110**, 076402 (2013).
- [14] M. Rossi, M. Retegan, C. Giacobbe, R. Fumagalli, A. Efimenko, T. Kulka, K. Wohlfeld, A. I. Gubanov, and M. Moretti Sala, *Possibility to realize spin-orbit-induced correlated physics in iridium fluorides*, Phys. Rev. B **95**, 235161 (2017).
- [15] A. A. Aczel, J. P. Clancy, Q. Chen, H. D. Zhou, D. Reig-Plessis, G. J. MacDougall, J. P. C. Ruff, M. H. Upton, Z. Islam, T. J. Williams, S. Calder, and J.-Q. Yan, *Revisiting the Kitaev material candidacy of Ir^{4+} double perovskite iridates*, Phys. Rev. B **99**, 134417 (2019).
- [16] A. Revelli, C. C. Loo, D. Kiese, P. Becker, T. Fröhlich, T. Lorenz, M. Moretti Sala, G. Monaco, F. L. Buessen, J. Attig, M. Hermanns, S. V. Streltsov, D. I. Khomskii, J. van den Brink, M. Braden, P. H. M. van Loosdrecht, S. Trebst, A. Paramekanti, and M. Grüninger, *Spin-orbit entangled $j = 1/2$ moments in Ba_2CeIrO_6 : A frustrated fcc quantum magnet*, Phys. Rev. B **100**, 085139 (2019).
- [17] A. Ruiz, N. P. Breznay, M. Li, I. Rousochatzakis, A. Allen, I. Zinda, V. Nagarajan, G. Lopez, Z. Islam, M. H. Upton, J. Kim, A. H. Said, X.-R. Huang, T. Gog, D. Casa, R. J. Birgeneau, J. D. Koralek, J. G. Analytis, N. B. Perkins, and A. Frano, *Magnon-spinon dichotomy in the Kitaev hyperhoneycomb β - Li_2IrO_3* , Phys. Rev. B **103**, 184404 (2021).
- [18] A. de la Torre, B. Zager, F. Bahrami, M. DiScala, J. R. Chamorro, M. H. Upton, G. Fabbris, D. Haskel, D. Casa, T. M. McQueen, F. Tafti, and K. W. Plumb, *Enhanced hybridization in the electronic ground state of the intercalated honeycomb iridate $Ag_3LiIr_2O_6$* , Phys. Rev. B **104**, L100416 (2021).
- [19] W. Jin, S. H. Chun, J. Kim, D. Casa, J. P. C. Ruff, C. J. Won, K. D. Lee, N. Hur, and Y.-J. Kim, *Magnetic excitations in the double-perovskite iridates $La_2M'IrO_6$ ($M = Co, Ni, \text{ and } Zn$) mediated by 3d-5d hybridization*, Phys. Rev. B **105**, 054419 (2022).
- [20] M. Magnaterra, M. Moretti Sala, G. Monaco, P. Becker, M. Hermanns, P. Warzanowski, T. Lorenz, D. I. Khomskii, P. H. M. van Loosdrecht, J. van den Brink, and M. Grüninger, *RIXS interferometry and the role of disorder in the quantum magnet $Ba_3Ti_{3-x}Ir_xO_9$* , Phys. Rev. Research **5**, 013167 (2023).
- [21] A. de la Torre, B. Zager, F. Bahrami, M. H. Upton, J. Kim, G. Fabbris, G.-H. Lee, W. Yang, D. Haskel, F. Tafti, and K. W. Plumb, *Momentum-independent magnetic excitation continuum in the honeycomb iridate $H_3LiIr_2O_6$* , Nat. Commun. **14**, 5018 (2023).
- [22] Jungho Kim, D. Casa, M. H. Upton, T. Gog, Young-June Kim, J. F. Mitchell, M. van Veenendaal, M. Daghofer, J. van den Brink, G. Khaliullin, and B. J. Kim, *Magnetic Excitation Spectra of Sr_2IrO_4 Probed by Resonant Inelastic X-Ray Scattering: Establishing Links to Cuprate Superconductors*, Phys. Rev. Lett. **108**, 177003 (2012).
- [23] J. Kim, M. Daghofer, A.H. Said, T. Gog, J. van den Brink, G. Khaliullin, and B.J. Kim, *Excitonic quasiparticles in a spin-orbit Mott insulator*, Nat. Commun. **5**, 4453 (2014).
- [24] Jungho Kim, A. H. Said, D. Casa, M. H. Upton, T. Gog, M. Daghofer, G. Jackeli, J. van den Brink, G. Khaliullin, and B. J. Kim, *Large Spin-Wave Energy Gap in the Bilayer Iridate $Sr_3Ir_2O_7$: Evidence for Enhanced Dipolar Interactions Near the Mott Metal-Insulator Transition*, Phys. Rev. Lett. **109**, 157402 (2012).
- [25] M. Moretti Sala, V. Schnells, S. Boseggia, L. Simonelli, A. Al-Zein, J. G. Vale, L. Paolasini, E. C. Hunter, R. S. Perry, D. Prabhakaran, A. T. Boothroyd, M. Krisch, G. Monaco, H. M. Ronnow, D. F. McMorrow, and F. Mila, *Evidence of quantum dimer excitations in $Sr_3Ir_2O_7$* , Phys. Rev. B **92**, 024405 (2015).
- [26] X. Lu, P. Olalde-Velasco, Y. Huang, V. Bisogni, J. Pellicciari, S. Fatale, M. Dantz, J. G. Vale, E. C. Hunter, J. Chang, V. N. Strocov, R. S. Perry, M. Grioni, D. F. McMorrow, H. M. Ronnow, and T. Schmitt, *Dispersive magnetic and electronic excitations in iridate perovskites probed by oxygen K-edge resonant inelastic x-ray scattering*, Phys. Rev. B **97**, 041102(R) (2018).
- [27] A. Bertin, L. Kiefer, P. Becker, L. Bohatý, and M. Braden, *Rotational phase transitions in antiferromite-type osmate and iridate compounds*, J. Phys.: Condens. Matter **36**, 245402 (2024).
- [28] N. Khan, D. Prishchenko, Y. Skourski, V. G. Mazurenko, and A. A. Tsirlin, *Cubic symmetry and magnetic frustration on the fcc spin lattice in K_2IrCl_6* , Phys. Rev. B **99**, 144425 (2019).
- [29] D. Reig-i-Plessis, T. A. Johnson, K. Lu, Q. Chen, J. P. C. Ruff, M. H. Upton, T. J. Williams, S. Calder, H. D. Zhou, J. P. Clancy, A. A. Aczel, and G. J. MacDougall, *Structural, electronic, and magnetic properties of nearly ideal $J_{\text{eff}} = 1/2$ iridium halides*, Phys. Rev. Mater. **4**, 124407 (2020).
- [30] N. Khan, D. Prishchenko, M. H. Upton, V. G. Mazurenko, and A. A. Tsirlin, *Towards cubic symmetry for Ir^{4+} : Structure and magnetism of the antiferromite K_2IrBr_6* , Phys. Rev. B **103**, 125158 (2021).
- [31] S. Lee, B. H. Kim, M.-J. Seong, and K.-Y. Choi, *Noncubic local distortions and spin-orbit excitons in K_2IrCl_6* , Phys. Rev. B **105**, 184433 (2022).
- [32] F. Meggle, M. Mikuta, M. Saule, V. Hermann, N. Khan, A. A. Tsirlin, and C. A. Kuntscher, *Optical signatures of the $J_{\text{eff}} = 1/2$ state in Ir^{4+} halides*, Phys. Rev. B **107**, 235142 (2023).
- [33] L. Bhaskaran, A. N. Ponomaryov, J. Wosnitza, N. Khan, A. A. Tsirlin, M. E. Zhitomirsky, and S. A. Zvyagin, *Antiferromagnetic resonance in the cubic iridium hexahalides (NH_4) $_2IrCl_6$ and K_2IrCl_6* , Phys. Rev. B **104**, 184404 (2021).
- [34] P. Balla, Y. Iqbal, and K. Penc, *Degenerate manifolds, helimagnets, and multi-Q chiral phases in the classical Heisenberg antiferromagnet on the face-centered-cubic lattice*, Phys. Rev. Res. **2**, 043278 (2020).
- [35] N. Iwahara and W. Furukawa, *Vibronic effect on resonant inelastic x-ray scattering in cubic iridium hexahalides*, Phys. Rev. B **108**, 075136 (2023).
- [36] E. M. Plotnikova, M. Daghofer, J. van den Brink, and K. Wohlfeld, *Jahn-Teller Effect in Systems with Strong On-Site Spin-Orbit Coupling*, Phys. Rev. Lett. **116**, 106401 (2016).
- [37] M. Moretti Sala, K. Ohgushi, A. Al-Zein, Y. Hirata, G. Monaco, and M. Krisch, *$CaIrO_3$: A Spin-Orbit Mott Insulator Beyond the $j_{\text{eff}} = 1/2$ Ground State*, Phys. Rev. Lett. **112**, 176402 (2014).
- [38] P. Warzanowski, N. Borgwardt, K. Hopfer, J. Attig, T. C. Koethe, P. Becker, V. Tsurkan, A. Loidl, M. Hermanns, P. H. M. van Loosdrecht, and M. Grüninger, *Multiple spin-orbit excitons and the electronic structure of α - $RuCl_3$* , Phys. Rev. Res. **2**, 042007(R) (2020).
- [39] J.-H. Lee, Y. Choi, S.-H. Do, B. H. Kim, M.-J. Seong,

- and K.-Y. Choi, *Multiple spin-orbit excitons in α -RuCl₃ from bulk to atomically thin layers*, npj Quantum Mater. **6**, 43 (2021).
- [40] J. G. Vale, C. D. Dashwood, E. Paris, L. S. I. Veiga, M. Garcia-Fernandez, A. Nag, A. Walters, K.-J. Zhou, I.-M. Pietsch, A. Jesche, P. Gegenwart, R. Coldea, T. Schmitt, and D. F. McMorrow, *High-resolution resonant inelastic x-ray scattering study of the electron-phonon coupling in honeycomb α -Li₂IrO₃*, Phys. Rev. B **100**, 224303 (2019).
- [41] S. Agrestini, F. Borgatti, P. Florio, J. Frassinetti, D. Fiore Mosca, Q. Faure, B. Detlefs, C. J. Sahle, S. Francoual, J. Choi, M. Garcia-Fernandez, K. -J. Zhou, V. F. Mitrovic, P. M. Woodward, G. Ghiringhelli, C. Franchini, F. Boscherini, S. Sanna, and M. Moretti Sala, *The origin of magnetism in a supposedly nonmagnetic osmium oxide*, arXiv:2401.12035, Phys. Rev. Lett. (in press, 2024).
- [42] A. Revelli, M. Moretti Sala, G. Monaco, C. Hickey, P. Becker, F. Freund, A. Jesche, P. Gegenwart, T. Eschmann, F. L. Buessen, S. Trebst, P. H. M. van Loosdrecht, J. van den Brink, and M. Grüninger, *Fingerprints of Kitaev physics in the magnetic excitations of honeycomb iridates*, Phys. Rev. Research **2**, 043094 (2020).
- [43] J. J. Lee, B. Moritz, W. S. Lee, M. Yi, C. J. Jia, A. P. Sorini, K. Kudo, Y. Koike, K. J. Zhou, C. Monney, V. Strocov, L. Patthey, T. Schmitt, T. P. Devereaux, and Z. X. Shen, *Charge-orbital-lattice coupling effects in the dd excitation profile of one-dimensional cuprates*, Phys. Rev. B **89**, 041104(R) (2014).
- [44] N. Iwahara and S. Shikano, *Vibronic excitations in resonant inelastic x-ray scattering spectra of K₂RuCl₆*, Phys. Rev. Res. **5**, 023051 (2023).
- [45] H. Takahashi, H. Suzuki, J. Bertinshaw, S. Bette, C. Mühle, J. Nuss, R. Dinnebi, A. Yaresko, G. Khaliullin, H. Gretarsson, T. Takayama, H. Takagi, and B. Keimer, *Nonmagnetic J = 0 State and Spin-Orbit Excitations in K₂RuCl₆*, Phys. Rev. Lett. **127**, 227201 (2021).
- [46] F. I. Frontini, G. H. J. Johnstone, N. Iwahara, P. Bhattacharyya, N. A. Bogdanov, L. Hozoi, M. H. Upton, D. M. Casa, D. Hirai, and Y.-J. Kim, *Spin-orbit-lattice entangled state in A₂MgReO₆ (A = Ca, Sr, Ba) revealed by resonant inelastic x-ray scattering*, arXiv:2311.01621, Phys. Rev. Lett. (in press, 2024).
- [47] F. Hennies, A. Pietzsch, M. Berglund, A. Föhlisch, Th. Schmitt, V. Strocov, H. O. Karlsson, J. Andersson, and J.-E. Rubensson, *Resonant Inelastic Scattering Spectra of Free Molecules with Vibrational Resolution*, Phys. Rev. Lett. **104**, 193002 (2010).
- [48] B. Henderson and G. F. Imbusch, *Optical spectroscopy of inorganic solids* (Oxford, 1989).
- [49] B. N. Figgis and M. A. Hitchman, *Ligand Field Theory and its Applications* (Wiley, 1999).
- [50] C. F. Ballhausen, *Introduction to Ligand Field Theory* (McGraw-Hill, New York, 1962).
- [51] R. Rückamp, E. Benckiser, M. W. Haverkort, H. Roth, T. Lorenz, A. Freimuth, L. Jongen, A. Möller, G. Meyer, P. Reutler, B. Büchner, A. Revcolevschi, S.-W. Cheong, C. Sekar, G. Krabbes, and M. Grüninger, *Optical study of orbital excitations in transition-metal oxides*, New J. Phys. **7**, 144 (2005).
- [52] P. Warzanowski, M. Magnaterra, G. Schlicht, Q. Faure, Ch. J. Sahle, P. Becker, L. Bohatý, M. Moretti Sala, G. Monaco, M. Hermanns, P.H.M. van Loosdrecht, and M. Grüninger, *Spin-orbit coupling in a half-filled t_{2g} shell: the case of 5d³ K₂ReCl₆*, Phys. Rev. B **109**, 155149 (2024).
- [53] P. Warzanowski, M. Magnaterra, P. Stein, G. Schlicht, Q. Faure, Ch. J. Sahle, T. Lorenz, P. Becker, L. Bohatý, M. Moretti Sala, G. Monaco, P. H. M. van Loosdrecht, and M. Grüninger, *Electronic excitations in 5d⁴ J = 0 Os⁴⁺ halides studied by resonant inelastic x-ray scattering and optical spectroscopy*, Phys. Rev. B **108**, 125120 (2023).
- [54] A. H. Cooke, R. Lazenby, F. R. McKim, J. Owen, and W. P. Wolf, *Exchange interactions in antiferromagnetic salts of iridium II. Magnetic susceptibility measurements*, Proc. R. Soc. London Ser. A **250**, 97 (1959).
- [55] M. Moretti Sala, C. Henriquet, L. Simonelli, R. Verbeni, and G. Monaco, *High energy-resolution set-up for Ir L₃ edge RIXS experiments*, J. Electron Spectrosc. Relat. Phenom. **188**, 150 (2013).
- [56] M. Moretti Sala, K. Martel, C. Henriquet, A. Al Zein, L. Simonelli, Ch.J. Sahle, H. Gonzalez, M.-C. Lagier, C. Ponchut, S. Huotari, R. Verbeni, M. Krisch, and G. Monaco, *A high-energy-resolution resonant inelastic X-ray scattering spectrometer at ID20 of the European Synchrotron Radiation Facility*, J. Synchrotron Rad. **25**, 580 (2018).
- [57] R. M. A. Azzam and N. M. Bashara, *Ellipsometry and Polarized Light* (Elsevier, New York, 1987).
- [58] J. W. Lynn, H. H. Patterson, G. Shirane, and R. G. Wheeler, *Soft rotary mode and structural phase transition in K₂ReCl₆*, Solid State Commun. **27**, 859 (1978).
- [59] D. Mintz, R. L. Armstrong, B. M. Powell, and W. J. L. Buyers, *Soft rotary mode in the antiferromagnetic K₂OsCl₆*, Phys. Rev. B **19**, 448, (1979).
- [60] G. P. O'Leary and R. G. Wheeler, *Phase Transitions and Soft Librational Modes in Cubic Crystals*, Phys. Rev. B **1**, 4409 (1970).
- [61] P. Schweiss, W. Reichardt, M. Braden, G. Collin, G. Heger, H. Claus, and A. Erb, *Static and dynamic displacements in RBa₂Cu₃O_{7- δ} (R=Y, Ho; $\delta = 0.05, 0.5$): A neutron-diffraction study on single crystals*, Phys. Rev. B **49**, 1387 (1994).
- [62] G.A. Sawatzky, *Testing Fermi-liquid models*, Nature **342**, 480 (1989).
- [63] M. A. Hitchman and P. J. Cassidy, *Polarized Crystal Spectrum of Bis(methylphenethylammonium) Tetrachlorocuprate(II): Analysis of the Energies, Vibrational Fine Structure, and Temperature Dependence of the "d-d" Transitions of the Planar CuCl₄²⁻ Ion*, Inorg. Chem. **18**, 1745 (1979).
- [64] D.M. Adams and H.A. Gebbie, *Absorption spectra of some inorganic complex halides by far infra-red interferometry*, Spectrochim. Acta **19**, 925 (1963).
- [65] G.L. Bottger and A.E. Salwin, *The vibrational spectra of alkali salts of hexahaloiridates*, Spectrochim. Acta **28A**, 925 (1972).
- [66] S. F. Parker and J. B. Forsyth. *K₂MCl₆ (M = Pt, Ir), location of the silent modes and forcefields*, J. Chem. Soc., Faraday Trans. **94**, 1111 (1998).
- [67] T.A. Keiderling, P.J. Stephens, S.B. Piepho, J.L. Slater, P.N. Schatz, *Infrared absorption and magnetic circular dichroism of Cs₂ZrCl₆:Ir⁴⁺*, Chem. Phys. **11**, 343 (1975).
- [68] R. K. Yoo and T. A. Keiderling, *Intraconfigurational absorption spectroscopy of IrCl₆²⁻ and IrBr₆²⁻ in A₂MX₆-type host crystals*, Chem. Phys. **108**, 317 (1986).
- [69] L. Pross, K. Rössler, and H. J. Schenk, *Optical studies on Hexahaloiridates - I Low temperature absorption spectra of K₂[ReCl₆] single crystals*, J. inorg. nucl. Chem. **36**, 155149 (2024).

- 317 (1974).
- [70] R.K. Yoo, S.C. Lee, B.A. Kozikowski and T.A. Keiderling, *Intraconfigurational absorption spectroscopy of $ReCl_6^{2-}$ in various A_2MCl_6 host crystals*, Chem. Phys. **117**, 237 (1987).
- [71] M. Bettinelli and C. D. Flint, *Magnon sidebands and cooperative absorptions in K_2ReCl_6 and Cs_2ReCl_6* , J. Phys. C: Solid State Phys. **21**, 5499 (1988).
- [72] B. A. Kozikowski and T. A. Keiderling, *Intraconfigurational absorption spectroscopy of Os^{4+} ion in K_2SnCl_6 and K_2OsCl_6 crystals*, J. Phys. Chem. **87**, 4630 (1983).
- [73] K. Huang and A. Rhys, *Theory of light absorption and non-radiative transitions in F-centres*, Proc. R. Soc. Lond. A **204**, 406 (1950).
- [74] L. J. P. Ament, M. van Veenendaal, and J. van den Brink, *Determining the electron-phonon coupling strength from Resonant Inelastic X-ray Scattering at transition metal L-edges*, EPL **95**, 27008 (2011).
- [75] A. Geondzhian and K. Gilmore, *Generalization of the Franck-Condon model for phonon excitations by resonant inelastic x-ray scattering*, Phys. Rev. B **101**, 214307 (2020).
- [76] K. Gilmore, *Quantifying vibronic coupling with resonant inelastic X-ray scattering*, Phys. Chem. Chem. Phys. **25**, 217 (2023).
- [77] L. Braicovich, M. Rossi, R. Fumagalli, Y. Peng, Y. Wang, R. Arpaia, D. Betto, G.M. De Luca, D. Di Castro, K. Kummer, M. Moretti Sala, M. Pagetti, G. Balestrino, N.B. Brookes, M. Salluzzo, S. Johnston, J. van den Brink, and G. Ghiringhelli, *Determining the electron-phonon coupling in superconducting cuprates by resonant inelastic x-ray scattering: Methods and results on $Nd_{1+x}Ba_{2-x}Cu_3O_{7-\delta}$* , Phys. Rev. Research **2**, 023231 (2020).
- [78] A. M. Black and C. D. Flint, *Jahn-Teller effect in the Γ_8 ($^2T_{2g}$, t_{2g}^3) state of $ReBr_6^{2-}$* , J. Chem. Soc., Faraday Trans. 2, **71**, 1871 (1975).
- [79] H. Liu and G. Khaliullin, *Pseudo-Jahn-Teller Effect and Magnetoelastic Coupling in Spin-Orbit Mott Insulators*, Phys. Rev. Lett. **122**, 057203 (2019).
- [80] L.J.P. Ament, M. van Veenendaal, T.P. Devereaux, J.P. Hill, and J. van den Brink, *Resonant inelastic x-ray scattering studies of elementary excitations*, Rev. Mod. Phys. **83**, 705 (2011).
- [81] T. P. Devereaux, A. M. Shvaika, K. Wu, K. Wohlfeld, C. J. Jia, Y. Wang, B. Moritz, L. Chaix, W.-S. Lee, Z.-X. Shen, G. Ghiringhelli, and L. Braicovich, *Directly Characterizing the Relative Strength and Momentum Dependence of Electron-Phonon Coupling Using Resonant Inelastic X-Ray Scattering*, Phys. Rev. X **6**, 041019 (2016).
- [82] S. Johnston, C. Monney, V. Bisogni, K.-J. Zhou, R. Kraus, G. Behr, V.N. Strocov, J. Málek, S.-L. Drechsler, J. Geck, Th. Schmitt, and J. van den Brink, *Electron-lattice interactions strongly renormalize the charge-transfer energy in the spin-chain cuprate Li_2CuO_2* , Nat. Commun. **7**, 10563 (2015).
- [83] E. Benckiser, R. Rückamp, T. Möller, T. Taetz, A. Möller, A. A. Nugroho, T. T. M. Palstra, G. S. Uhrig, and M. Grüninger, *Collective orbital excitations in orbitally ordered YVO_3 and $HoVO_3$* , New J. Phys. **10**, 053027 (2008).
- [84] G.M. Sheldrick, *SHELXT – Integrated space-group and crystal-structure determination*, Acta Cryst. A **71**, 3 (2015).
- [85] G.M. Sheldrick, *Crystal structure refinement with SHELXL*, Acta Cryst. C **71**, 3 (2015).
- [86] Joint CCDC/FIZ Karlsruhe deposition service, www.ccdc.cam.ac.uk/discover/news/2018-07-new-joint-services/
- [87] G. Khaliullin, P. Horsch, and A. M. Oleś, *Theory of optical spectral weights in Mott insulators with orbital degrees of freedom*, Phys. Rev. B **70**, 195103 (2004).
- [88] A. M. Oleś, G. Khaliullin, P. Horsch, and L. F. Feiner, *Fingerprints of spin-orbital physics in cubic Mott insulators: Magnetic exchange interactions and optical spectral weights*, Phys. Rev. B **72**, 214431 (2005).
- [89] Z. Fang, N. Nagaosa, and K. Terakura, *Anisotropic optical conductivities due to spin and orbital ordering in $LaVO_3$ and YVO_3 : First-principles studies*, Phys. Rev. B **67**, 035101 (2003).
- [90] N. N. Kovaleva, A. V. Boris, C. Bernhard, A. Kulkov, A. Pimenov, A. M. Balbashov, G. Khaliullin, and B. Keimer, *Spin-Controlled Mott-Hubbard Bands in $LaMnO_3$ Probed by Optical Ellipsometry*, Phys. Rev. Lett. **93**, 147204 (2004).
- [91] J. S. Lee, M. W. Kim, and T. W. Noh, *Optical excitations of transition-metal oxides under the orbital multiplicity effects*, New J. Phys. **7**, 147 (2005).
- [92] A. Gössling, R. Schmitz, H. Roth, M.W. Haverkort, T. Lorenz, J.A. Mydosh, E. Müller-Hartmann, and M. Grüninger, *Mott-Hubbard exciton in the optical conductivity of $YTiO_3$ and $SmTiO_3$* , Phys. Rev. B **78**, 075122 (2008).
- [93] J. Reul, A. A. Nugroho, T. T. M. Palstra, and M. Grüninger, *Probing orbital fluctuations in RVO_3 ($R = Y, Gd, \text{ or } Ce$) by ellipsometry*, Phys. Rev. B **86**, 125128 (2012).
- [94] I. Vergara, M. Magnaterra, P. Warzanowski, J. Attig, S. Kunkemöller, D.I. Khomskii, M. Braden, M. Hermanns, and M. Grüninger, *Spin-orbit coupling and crystal-field splitting in Ti-doped Ca_2RuO_4 studied by ellipsometry*, Phys. Rev. B **106**, 085103 (2022).
- [95] G. Zhang and E. Pavarini, *Mott transition, spin-orbit effects, and magnetism in Ca_2RuO_4* , Phys. Rev. B **95**, 075145 (2017).
- [96] B. H. Kim, G. Khaliullin, and B. I. Min, *Electronic excitations in the edge-shared relativistic Mott insulator: Na_2IrO_3* , Phys. Rev. B **89**, 081109(R) (2014).
- [97] S. M. Winter, A. A. Tsirlin, M. Daghofer, J. van den Brink, Y. Singh, P. Gegenwart, and R. Valentí, *Models and materials for generalized Kitaev magnetism*, J. Phys.: Condens. Matter **29**, 493002 (2017).
- [98] Z. Alpichshev, F. Mahmood, G. Cao, and N. Gedik, *Confinement-Deconfinement Transition as an Indication of Spin-Liquid-Type Behavior in Na_2IrO_3* , Phys. Rev. Lett. **114**, 017203 (2015).
- [99] O. Mehio, X. Li, H. Ning, Z. Lenarčič, Y. Han, M. Buchhold, Z. Porter, N. J. Laurita, S. D. Wilson, and D. Hsieh, *A Hubbard exciton fluid in a photo-doped antiferromagnetic Mott insulator*, Nat. Phys. **19**, 1876 (2023).